Supplement of Atmos. Chem. Phys., 24, 6071–6093, 2024
https://doi.org/10.5194/acp-24-6071-2024-supplement

Atmospheric Chemistry and Physics
Open Access

Supplement of

Global aviation contrail climate effects from 2019 to 2021

Roger Teoh et al.

Correspondence to: Marc E. J. Stettler (m.stettler@imperial.ac.uk)

Table of Contents

S1 Meteorology

S1.1 ERA5 high-resolution realization

In this study, we use meteorological and radiation data from the European Centre for Medium-Range Weather Forecast (ECMWF) Reanalysis 5th Generation (ERA5) high-resolution realization (HRES) to perform the global contrail simulation (Hersbach et al., 2020). The ERA5 HRES is publicly available from the ECMWF Copernicus Climate Data Store (ECMWF, 2021) and the following variables were downloaded at a spatiotemporal resolution of 0.25° × 0.25° over 37 pressure levels for meteorological variables (or 1 level for radiation variables) and at a 1 h temporal resolution:

- specific humidity (in kg kg^{-1}),
- air temperature (in K),
- eastward and northward wind (in m s^{-1}),
- lagrangian tendency of air pressure, i.e., vertical velocity (in Pa s^{-1}),
- specific cloud ice water content (in kg kg^{-1}),
- fraction of cloud cover,
- geopotential (in m^2 s^{-2}),
- top of atmosphere incident solar radiation (in J m^{-2}),
- top of atmosphere net upward shortwave flux (in J m^{-2}), and
- top of atmosphere outgoing longwave flux (in J m^{-2}).

Meteorology at each waypoint is obtained using a quadrilinear interpolation across space (longitude, latitude, and pressure level) and time. We calculate the relative humidity with respect to liquid water (RH) and relative humidity with respect to ice (RHi) using the following equations from Sonntag (1994),

$$\mathrm{RH} = \frac{p_{\mathrm{w}} q_{\mathrm{w}} R_1}{p_{\mathrm{liq}} R_0}, \tag{S1}$$

$$\mathrm{RHi} = \frac{p_{\mathrm{w}} q_{\mathrm{w}} R_1}{p_{\mathrm{ice}} R_0}. \tag{S2}$$

where p_{w} is the pressure altitude for each waypoint (in Pa), q_{w} is the specific humidity, R_0 (287.05 J kg^{-1} K^{-1}) and R_1 (461.51 J kg^{-1} K^{-1}) are the real gas constant for air and water vapour respectively, and the saturation pressure of water vapour over liquid water (p_{liq}, in Pa) and ice (p_{ice}, in Pa) are calculated based on air temperature (T_{w}) (Sonntag, 1994),

$$p_{\mathrm{liq}} = 100 \exp\left[\frac{-6096.9385}{T_{\mathrm{w}}} + 16.635794 - 0.02711193 T_{\mathrm{w}} + (1.673952 \times 10^{-5}) {T_{\mathrm{w}}}^2 + 2.433502 \ln(T_{\mathrm{w}})\right], \tag{S3}$$

$$p_{\mathrm{ice}} = 100 \exp\left[\frac{-6024.5282}{T_{\mathrm{w}}} + 24.721994 + 0.010613868 T_{\mathrm{w}} - (1.3198825 \times 10^{-5}) {T_{\mathrm{w}}}^2 - 0.49382577 \ln(T_{\mathrm{w}})\right]. \tag{S4}$$

The simulated contrail properties and lifetime have been shown to be highly sensitive to the RHi (Schumann et al., 2021; Teoh et al., 2022). However, existing studies have identified several limitations in the humidity fields provided by ECMWF ERA5 products. An assessment of the ERA5 humidity fields showed that the ERA5-derived ice supersaturated regions (ISSR) coverage area could be overestimated by up to 100% when compared with radiosonde measurements (Agarwal et al., 2022), or underestimated relative to in-situ humidity measurements from the In-Service Aircraft for a Global Observing System (IAGOS) campaign (Reutter et al., 2020). In addition, the magnitude of RHi within the ERA5-derived ISSR are generally weakly supersaturated (RHi ≈ 100%) and do not generally exceed RHi > 120% (Reutter et al., 2020; Gierens et al., 2020; Teoh et al., 2022). The low variability in RHi magnitude is most likely caused by simplified assumptions adopted in the ERA5 products where the relaxation time, i.e., time required for the excess supersaturated humidity to be deposited into ambient particles and ice crystals and reach equilibrium (RHi ≈ 100%), is currently set to one model time step (Tompkins et al., 2007; Koop et al., 2000). In addition, the spatiotemporal resolution of existing meteorological datasets is not sufficient to capture the sub-grid scale variability and localised air pockets with RHi > 120%. Therefore, the use of

ERA5 products for contrail simulation can lead to errors and uncertainties in the simulated contrail lifetime, properties, and climate forcing (Teoh et al., 2022; Agarwal et al., 2022; Gierens et al., 2020).

S1.2 Existing corrections to ERA5 humidity fields

Studies that simulated contrails with the contrail cirrus prediction model (CoCiP) have formulated different approaches to account for the known limitations in the humidity fields provided by ECMWF products. Earlier studies used an enhancement factor (RHi_c) to uniformly increase the RHi (Schumann, 2012; Schumann et al., 2015; Teoh et al., 2020; Schumann et al., 2021),

$$\mathrm{RHi}_{\mathrm{Corrected}} = \frac{\mathrm{RHi}}{\mathrm{RHi_c}}, \quad \text{(S5)}$$

where the RHi_c was set to 0.90 or 0.95 depending on the ECMWF product used (reanalysis/forecast), its spatiotemporal resolution, and/or the spatial domain of the simulation. While the rationale of Eq. (S5) was to increase the mean RHi so that the corrected humidity fields are no longer weakly supersaturated, there are inherent limitations where: (i) the correction could overestimate the ISSR coverage area, and subsequent estimates of the simulated contrail formation, lifetime and climate forcing (Agarwal et al., 2022); and (ii) it does not produce an RHi distribution that is consistent with in-situ measurements from the IAGOS campaign (Teoh et al., 2022).

To address these issues, Teoh et al. (2022) used in-situ humidity measurements from the IAGOS campaign (Petzold et al., 2020; Boulanger et al., 2022) to develop a new humidity correction methodology for the North Atlantic region,

$$\mathrm{RHi}_{\mathrm{corrected}} = \begin{cases} \dfrac{\mathrm{RHi}}{a_{\mathrm{opt}}} & , \mathrm{when} \left(\dfrac{\mathrm{RHi}}{a_{\mathrm{opt}}}\right) \leq 1 \\ \min\left(\left(\dfrac{\mathrm{RHi}}{a_{\mathrm{opt}}}\right)^{b_{\mathrm{opt}}}, \mathrm{RHi}_{\mathrm{max}}\right) & , \mathrm{when} \left(\dfrac{\mathrm{RHi}}{a_{\mathrm{opt}}}\right) > 1 \end{cases} \tag{S6}$$

where $\mathrm{RHi}_{\mathrm{max}}$ = 1.65, a_{opt} = 0.9779 and b_{opt} = 1.635 are calibrated coefficients to minimise the Cramer-von Mises (CvM) test statistic, a measure of the goodness of fit between two probability density functions (Parr and Schucany, 1980). This correction methodology addresses the two limitations from the earlier approach, i.e. Eq. (S5), where: (i) the false positive ($\mathrm{N}_{\mathrm{IAGOS}}/\mathrm{Y}_{\mathrm{HRES}}$, i.e., the ERA5 HRES derived RHi indicates that the waypoint is in ISSR but not in the IAGOS measurements) and false negative ($\mathrm{Y}_{\mathrm{IAGOS}}/\mathrm{N}_{\mathrm{HRES}}$) rates are generally symmetrical which should lead to the cancelling out of errors in ISSR and contrail occurrence over the spatiotemporal domain; and (ii) the distribution of $\mathrm{RHi}_{\mathrm{corrected}}$ is now consistent with in-situ RHi measurements from IAGOS (refer to Fig. S9 in Teoh et al. (2022)). Using Eq. (S6), the 2019 annual mean contrail cirrus net radiative forcing (RF) over the North Atlantic increased from 121 mW m^{-2} (no humidity correction) to 235 mW m^{-2}, indicating that the simulated contrail climate forcing is highly sensitive to the provided humidity fields (Teoh et al., 2022). However, we also note that the correction was formulated using RHi measurements in the North Atlantic and therefore, the calibrated coefficients (a_{opt} and b_{opt}) might not be valid when applied across the globe.

S1.3 Global humidity correction

Here, we use the full (global) IAGOS dataset (Petzold et al., 2020; Boulanger et al., 2022) to extend the humidity correction methodology from Teoh et al. (2022) so it can be applied to the global contrail simulation. The IAGOS dataset provides the aircraft position (longitude, latitude, pressure level and time) and measurements of q_{w} and T_{w} at a ~4 s time interval from 2,161 distinct flights in 2019. For each flight, we excluded waypoints that are below 25,000 feet and resampled the time series data to obtain the mean q_{w} and T_{w} at a frequency of 60 s to minimise the autocorrelation between data points (Gierens et al., 2020), and the resampled dataset consists of 682,308 unique waypoints. Fig. S1 and S2 shows the spatial distribution of the waypoints where q_w and T_w were measured: ~95% of the data points were measured in the Northern Hemisphere, of which ~63% of them were between 20–50°N, and ~69% of the measurements were at altitudes between 35,000 and 40,000 feet.

Table S1: Comparison of the ISSR occurrence between the in-situ RHi measurements from the IAGOS campaign in 2019 versus the RHi derived from the ERA5 HRES: (a) without humidity correction; and (b) with the global humidity correction, c.f. Eq. (S6) to Eq. (S9). The comparison is segmented into latitude intervals of 10°. Y_{IAGOS} indicates that the waypoint has an RHi > 100% (ISSR occurrence) according to the in-situ measurements, while N_{IAGOS} indicates the opposite. The subscript "HRES" is used to indicate ISSR occurrence as provided by the ERA5 HRES. For (b), the metrics that are highlighted in green (red) indicates that its performance has improved (degraded) relative to (a).

	No. of waypoints	Y_{IAGOS}/Y_{HRES} (%)	N_{IAGOS}/N_{HRES} (%)	Y_{IAGOS}/N_{HRES} (%)	N_{IAGOS}/Y_{HRES} (%)	Ratio[a]	CvM stat[b]	ETS[c]
(a) IAGOS vs. ERA5 HRES (No RHi correction)								
0 - 10°N	20650	9.16	70.1	8.22	12.5	-0.341	58.2	0.207
10 - 20°N	48366	5.02	83.2	5.67	6.06	-0.064	73.0	0.246
20 - 30°N	144910	2.90	90.1	2.90	4.08	-0.290	43.7	0.264
30 - 40°N	141131	4.42	87.7	3.69	4.14	-0.110	93.1	0.322
40 - 50°N	114018	5.40	85.1	6.24	3.31	0.889	261	0.315
50 - 60°N	106993	6.75	83.1	6.39	3.73	0.714	232	0.347
60 - 90°N	33762	5.57	87.0	5.06	2.33	1.169	91.7	0.390
(b) IAGOS vs. ERA5 HRES (Global humidity correction)								
0 - 10°N	20650	7.82	71.8	9.56	10.9	-0.119	2.09	0.183
10 - 20°N	48366	4.44	84.1	6.25	5.21	0.199	2.55	0.229
20 - 30°N	144910	2.58	90.7	3.22	3.50	-0.080	9.93	0.249
30 - 40°N	141131	4.28	88.0	3.83	3.87	-0.010	24.2	0.319
40 - 50°N	114018	6.70	83. 7	4.94	4.69	0.054	1.06	0.358
50 - 60°N	106993	8.40	81.5	4.74	5.40	-0.122	22.3	0.394
60 - 90°N	33762	6.93	86.1	3.70	3.28	0.128	0.360	0.456

[a]: Ratio compares the false positive and false negative rate and is computed by $\left(\frac{Y_{IAGOS}/N_{HRES}\ (\%)}{N_{IAGOS}/Y_{HRES}\ (\%)} - 1\right)$. A positive value indicates that the ERA5 HRES underpredicts ISSR occurrence, a value of zero indicates a symmetrical false positive and false negative rate, while a negative value indicates that the ERA5 HRES overpredicts ISSR occurrence.

[b]: CvM test statistic, where a lower value indicates a better goodness-of-fit between the probability density function of the measured and ERA5-derived RHi.

[c]: The equitable threat score (ETS) is calculated according to Appendix A of Gierens et al. (2020), where ETS = 1 indicates that the ERA5-derived RHi is in perfect agreement with measurements, ETS = 0 indicates a completely random relationship, while ETS < 0 indicates an inverse relationship between the measured and ERA5-derived RHi.

The RHi for each waypoint is calculated using: (i) Eq. (S2) and (S4) with in-situ measurements of q_w and T_w, hereby known as RHi_{IAGOS}; and (ii) a quadrilinear interpolation from the ERA5 HRES humidity fields. To avoid statistical bias and oversampling at specific latitude bands, we split the IAGOS dataset into latitude bins of 10° intervals. Table S1a compares RHi_{IAGOS} with the RHi derived from the original ERA5 HRES humidity fields for each latitude bin. An analysis of the false positive (N_{IAGOS}/Y_{HRES}) and false negative (Y_{IAGOS}/N_{HRES}) rates shows that the RHi errors have a latitude dependence, where the ERA5-derived ISSR coverage area could be: (i) overpredicted at the tropics and subtropics (0–40°N); and (ii) underpredicted at higher latitudes above 40°N.

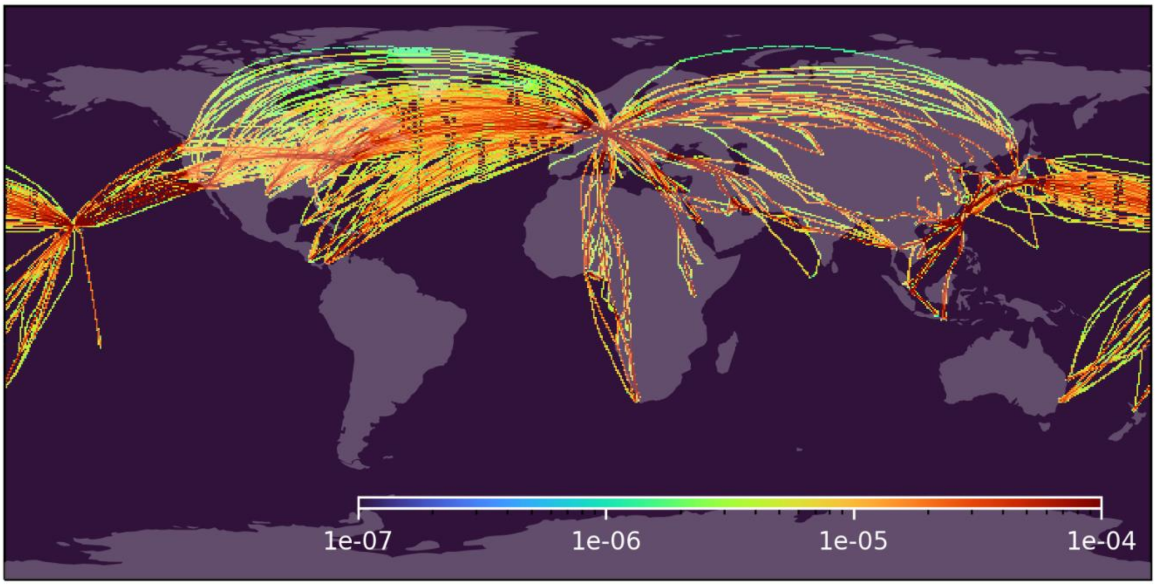

Figure S1: Spatial distribution of the data points provided by the resampled IAGOS dataset, where the colour bar represents the normalised density at each pixel (682,308 waypoints from 2,161 unique flights). Basemap plotted using Cartopy 0.22.0 and sourced from Natural Earth; licensed under public domain.

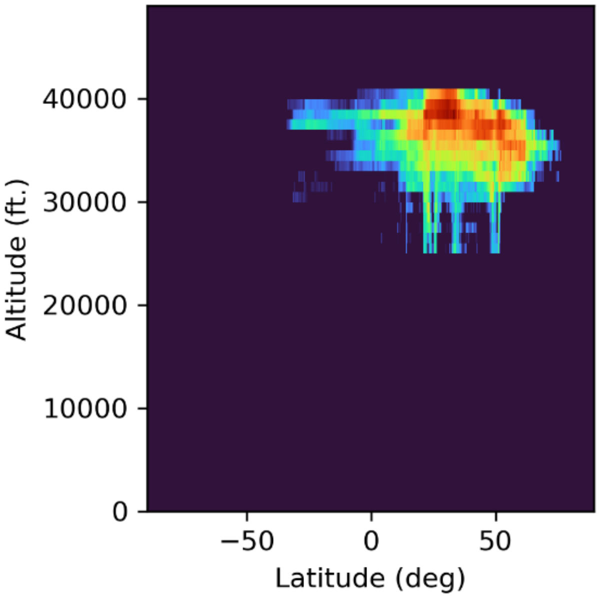

Figure S2: Distribution of the data points provided by the resampled IAGOS dataset by latitude and altitude (682,308 waypoints from 2,161 unique flights).

Table S2: a_{opt} and b_{opt} coefficients for each latitude band that is calibrated using the full IAGOS dataset and a bootstrap resampling method (n=1000) that provides an estimate of their respective standard errors.

	a_{opt}		b_{opt}	
	Full dataset	**Bootstrap**[a]	**Full dataset**	**Bootstrap**[a]
0 - 10°N	1.022	1.038 [1.019, 1.056]	2.900[b]	2.900[b]
10 - 20°N	1.003	1.023 [1.013, 1.034]	2.672	2.664 [2.539, 2.813]
20 - 30°N	1.020	1.019 [1.013, 1.025]	1.516	1.519 [1.453, 1.586]
30 - 40°N	1.007	1.011 [1.006, 1.019]	1.445	1.448 [1.398, 1.492]
40 - 50°N	0.9563	0.9644 [0.9547, 0.9750]	1.633	1.632 [1.594, 1.680]
50 - 60°N	0.9641	0.9782 [0.9688, 0.9875]	1.320	1.325 [1.289, 1.359]
60 - 90°N	0.9406	0.9099 [0.8734, 0.9430]	1.336	1.340 [1.266, 1.498]

[a]: The bootstrap resampling method is used to estimate the mean a_{opt} and b_{opt} for each latitude band and their respective standard error [1st percentile, 99th percentile].

[b]: The b_{opt} for this latitude band is constrained to 2.9 to prevent the corrected RHi in having unrealistic values.

Table S3: Comparison of different performance metrics to evaluate the agreement between the RHi measurements from the full IAGOS dataset for 2019 versus the uncorrected and corrected ERA5 HRES global humidity fields. These metrics are weighted by the number of waypoints in each latitude bin (see Table S1).

Full IAGOS dataset vs. ERA5 HRES	**Correct prediction (%)**	**Ratio**[a]	**Mean CvM statistic**[b]	**Mean ETS**[c]
Uncorrected humidity fields	90.9	0.245	134	0.305
Global humidity correction	91.1	-0.014	12.4	0.319
North Atlantic correction (Teoh et al., 2022)	90.7	-0.104	45.0	0.324

[a]: Ratio compares the false positive and false negative rate and is computed by $\left(\frac{Y_{IAGOS}/N_{HRES}\ (\%)}{N_{IAGOS}/Y_{HRES}\ (\%)} - 1\right)$. A positive value indicates that the ERA5 HRES underpredicts ISSR occurrence, a value of zero indicates a symmetrical false positive and false negative rate, while a negative value indicates that the ERA5 HRES overpredicts ISSR occurrence.

[b]: CvM test statistic, where a lower value indicates a better goodness-of-fit between the probability density function of the measured and ERA5-derived RHi.

[c]: The equitable threat score (ETS) is calculated according to Appendix A of Gierens et al. (2020), where ETS = 1 indicates that the ERA5-derived RHi is in perfect agreement with measurements, ETS = 0 indicates a completely random relationship, while ETS < 0 indicates an inverse relationship between the measured and ERA5-derived RHi.

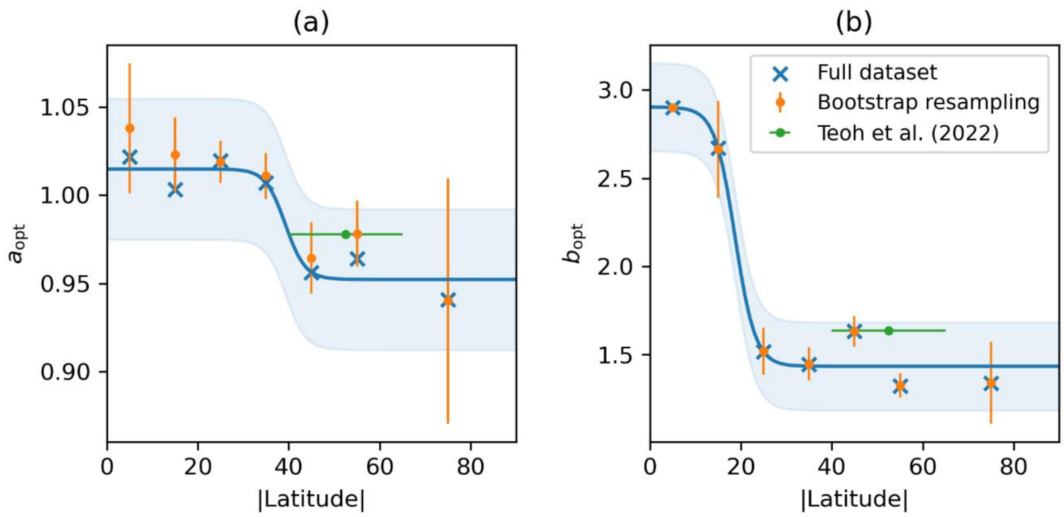

Figure S3: Visualisation of Eq. (S7) and (S8), where a sigmoid is used to fit (a) a_{opt} and (b) b_{opt} as a function of latitude. The vertical lines from the bootstrap resampling method (orange data points) represent the 1st and 99th percentile of the standard error, and the shaded regions approximate the uncertainty of a_{opt} and b_{opt}. The a_{opt} and b_{opt} derived from an earlier study in the North Atlantic region (Teoh et al., 2022) **is also plotted as green data points.**

Based on these results, we use Eq. (S6) as a basis to extend the humidity correction methodology from Teoh et al. (2022) and capture these latitude effects. The a_{opt} and b_{opt} coefficients are optimised for each latitude bin: the first step involves optimising a_{opt} with the objective function of yielding a symmetrical false positive and false negative rate so that errors in the ISSR occurrence cancel each other out; and b_{opt} is then optimised by minimising the CvM test statistic (Parr and Schucany, 1980) so that the ERA5-derived RHi has a probability density function that is consistent with $\mathrm{RHi}_{\mathrm{IAGOS}}$. Table S2 summarises the a_{opt} and b_{opt} coefficients for each latitude band that is calibrated using: (i) the full dataset; and (ii) a bootstrap resampling method that estimates their respective standard errors and used to approximate their uncertainty range. We then fit the a_{opt} and b_{opt} derived from the full dataset (Table S2) with a sigmoid function to account for the rapid change tropopause height between 20° and 50° N/S (Santer et al., 2003),

$$a_{\mathrm{opt}} = \frac{a_0}{1+\exp\left(a_1 \times (|\mathrm{lat}| - a_2)\right)} + a_3, \tag{S7}$$

$$b_{\mathrm{opt}} = \frac{b_0}{1+\exp\left(b_1 \times (|\mathrm{lat}| - b_2)\right)} + b_3, \tag{S8}$$

where $a_0 = 0.06262$, $a_1 = 0.4589$, $a_2 = 39.25$ and $a_3 = 0.9522 \pm 0.04$, and $b_0 = 1.471$, $b_1 = 0.4431$, $b_2 = 18.76$ and $b_3 = 1.433 \pm 0.25$. The range of a_3 and b_3 is specified to cover the uncertainty range of a_{opt} and b_{opt} that is derived from the bootstrap resampling method (Fig. S3). Given the limited number of waypoints below 0°N (< 5% of all data points in the IAGOS dataset), we use the absolute latitude values in Eq. (S7) and (S8) assuming that the latitude effects are symmetrical between the Northern and Southern Hemisphere. The $\mathrm{RHi}_{\mathrm{max}}$ term in Eq. (S6) is also revised and calculated as a function of T_{w} to ensure that the $\mathrm{RHi}_{\mathrm{corrected}}$ is within the maximum value permissible by thermodynamics (i.e., RH < 100%, and below the threshold that leads to homogeneous ice nucleation and formation of natural cirrus clouds) (Pruppacher et al., 2007; Kärcher and Lohmann, 2002; Tompkins et al., 2007),

$$\mathrm{RHi_{max}} = \begin{cases} \dfrac{p_{\mathrm{liq}}(T_\mathrm{w})}{p_{\mathrm{ice}}(T_\mathrm{w})} & \text{, when } T_\mathrm{w} > 235\ \mathrm{K} \\ 1.67 + (1.45 - 1.67) \times \dfrac{(T_\mathrm{w} - 190)}{(235 - 190)} & \text{, when } T_\mathrm{w} \leq 235\ \mathrm{K} \end{cases} \quad \text{(S9)}$$

where $p_{\mathrm{liq}}(T_\mathrm{w})$ and $p_{\mathrm{ice}}(T_\mathrm{w})$ are estimated using Eq. (S3) and (S4) respectively.

Table S4: Comparison of the ISSR occurrence between the in-situ RHi measurements from the IAGOS campaign in 2019 versus the RHi derived from the ERA5 HRES: (a) without humidity correction; and (b) with the global humidity correction, c.f. Eq. (S6) to Eq. (S9). The comparison is segmented into latitude intervals of 20° and altitude intervals of 4000 feet. Y_{IAGOS} indicates that the waypoint has an RHi > 100% (ISSR occurrence) according to the IAGOS measurements, while N_{IAGOS} indicates the opposite. The subscript "HRES" is used to indicate ISSR occurrence as provided by the ERA5 HRES. For (b), the metrics that are highlighted in green (red) indicates that its performance has improved (degraded) relative to (a).

	No. of waypoints	$Y_{\mathrm{IAGOS}}/Y_{\mathrm{HRES}}$ (%)	$N_{\mathrm{IAGOS}}/N_{\mathrm{HRES}}$ (%)	$Y_{\mathrm{IAGOS}}/N_{\mathrm{HRES}}$ (%)	$N_{\mathrm{IAGOS}}/Y_{\mathrm{HRES}}$ (%)	Ratio[a]	CvM stat[b]	ETS[c]
(a) IAGOS vs. ERA5 HRES (No RHi correction)								
0 - 20°N								
FL280-320	4615	5.26	81.0	8.21	5.53	0.486	12.5	0.217
FL320-360	19580	6.38	79.5	7.56	6.56	0.152	75.7	0.245
FL360-400	40529	6.60	78.5	5.96	8.98	-0.336	78.5	0.237
20 - 40°N								
FL280-320	15989	4.32	86.1	4.98	4.58	0.087	12.3	0.267
FL320-360	52857	5.08	86.6	4.97	3.31	0.502	104.0	0.338
FL360-400	184583	3.30	89.7	2.89	4.12	-0.297	53.5	0.289
40 - 60°N								
FL280-320	13867	12.9	72.1	10.2	4.86	1.089	97.2	0.369
FL320-360	79438	8.96	78.6	8.09	4.39	0.844	218.4	0.349
FL360-400	122404	3.41	89.1	4.76	2.71	0.755	172.4	0.280
(b) IAGOS vs. ERA5 HRES (Global humidity correction)								
0 - 20°N								
FL280-320	4615	4.46	81.6	9.01	4.88	0.849	5.78	0.187
FL320-360	19580	5.32	80.5	8.62	5.55	0.552	26.2	0.212
FL360-400	40529	5.90	79.6	6.66	7.80	-0.146	10.6	0.224
20 - 40°N								
FL280-320	15989	3.88	86.9	5.41	3.85	0.404	4.90	0.255
FL320-360	52857	4.70	87.0	5.36	2.94	0.824	63.5	0.321
FL360-400	184583	3.11	90.1	3.08	3.72	-0.171	7.79	0.283
40 - 60°N								
FL280-320	13867	15.2	70.3	7.82	6.71	0.166	5.73	0.412
FL320-360	79438	11.1	76.6	5.98	6.33	-0.056	14.4	0.397
FL360-400	122404	4.36	87.9	3.81	3.91	-0.025	2.06	0.323

[a]: Ratio compares the false positive and false negative rate and is computed by $\left(\frac{Y_{\mathrm{IAGOS}}/N_{\mathrm{HRES}}\ (\%)}{N_{\mathrm{IAGOS}}/Y_{\mathrm{HRES}}\ (\%)} - 1\right)$. A positive value indicates that the ERA5 HRES underpredicts ISSR occurrence, a value of zero indicates a symmetrical false positive and false negative rate, while a negative value indicates that the ERA5 HRES overpredicts ISSR occurrence.

[b]: CvM test statistic, where a lower value indicates a better goodness-of-fit between the probability density function of the measured and ERA5-derived RHi.

[c]: The equitable threat score (ETS) is calculated according to Appendix A of Gierens et al. (2020), where ETS = 1 indicates that the ERA5-derived RHi is in perfect agreement with measurements, ETS = 0 indicates a completely random relationship, while ETS < 0 indicates an inverse relationship between the measured and ERA5-derived RHi.

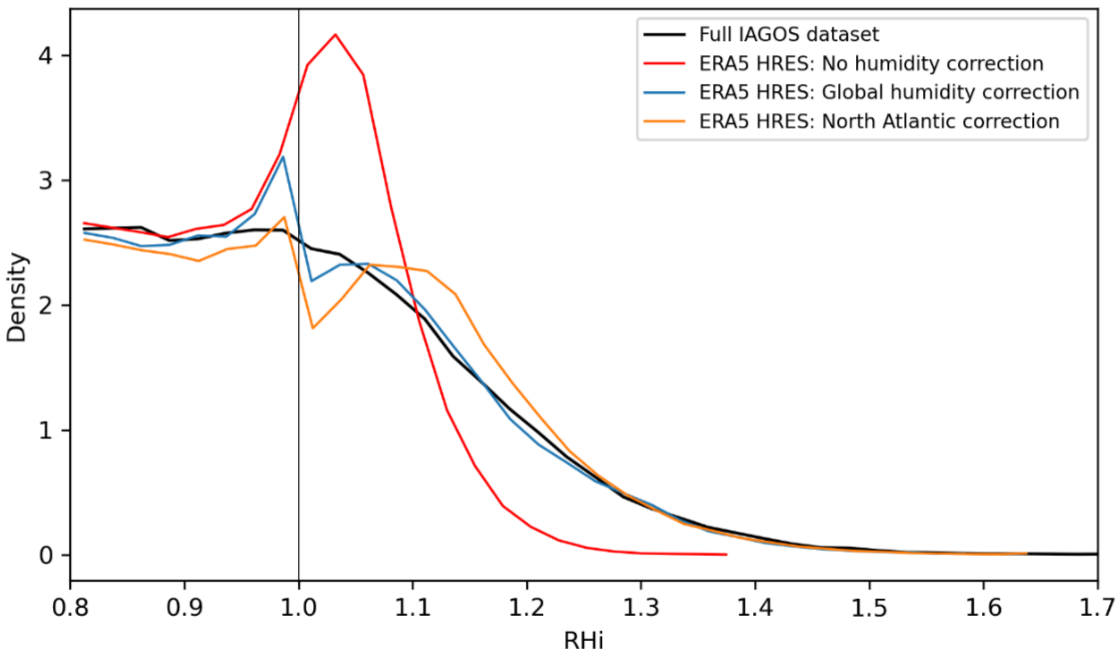

Figure S4: Probability density function of the RHi measurements provided by the full IAGOS dataset (black line) versus those derived from the ERA5 HRES with: (i) no humidity correction (red line); (ii) the global humidity correction (blue line); and (iii) the North Atlantic correction previously developed by Teoh et al. (2022) **(orange line).**

When evaluated using four different performance metrics, the global humidity correction generally improved the agreement between RHi_{IAGOS} and $RHi_{corrected}$ for each latitude bin (Table S1). Table S3 summarises the performance metrics when the full IAGOS dataset is compared with the uncorrected and corrected ERA5 HRES global humidity fields, showing that the weighted-mean:

i. percentage of waypoints with the correct prediction of ISSR occurrence (Y_{IAGOS}/Y_{HRES} and N_{IAGOS}/N_{HRES}) increased by 0.2% from 90.9% to 91.1%,
ii. false positive (N_{IAGOS}/Y_{HRES}) and false negative (Y_{IAGOS}/N_{HRES}) rates are now symmetrical, meaning that errors in the ISSR occurrence and persistent contrail formation are expected to cancel out over the spatiotemporal domain,
iii. CvM test statistic reduced by 91% (from 134 to 12.4), which implies a significant improvement in the goodness-of-fit between the probability density function of RHi_{IAGOS} and $RHi_{corrected}$ (Fig. S4), and

iv. ETS improved slightly by 4.4% from 0.305 to 0.319, but the comparison at 0 – 40°N latitudes showed that the global humidity correction lowered the weighted-mean ETS by 3.9% from 0.281 to 0.270 (Table S1).

To evaluate the agreement between RHi_{IAGOS} and $RHi_{corrected}$ at different altitudes, we also segmented the full IAGOS dataset by latitude intervals of 20° and altitude intervals of 4000 feet (Table S4). The results showed that:

i. the CvM test statistic improved across every latitude and altitude categories, suggesting an improved goodness-of-fit between the probability density function of RHi_{IAGOS} and $RHi_{corrected}$, but
ii. the weighted-mean ETS degraded from 0.286 to 0.275 (-3.8%) across all altitude intervals at lower latitudes (0 – 40°N), and
iii. the weighted-mean ratio of false negative-to-false positive rate ($\frac{Y_{IAGOS}/N_{HRES}\ (\%)}{N_{IAGOS}/Y_{HRES}\ (\%)} - 1$) at lower latitudes (0 – 40°N) and altitudes (28,000 – 36,000 feet) increased by around two-fold from 0.356 (no humidity correction) to 0.670 (with global humidity corrections applied). In other words, the uncorrected humidity fields are already underestimating the ISSR occurrence in this region (0 – 40°N and 28,000 – 36,000 feet); and applying the global humidity correction could potentially worsen this underestimation.

Points (ii) and (iii) suggest that there could be potential limitations in the global humidity correction when applied at lower latitudes (0 – 40°N) and altitudes (28,000 – 36,000 feet), where the air traffic activity in this region (0 – 40°N and 28,000 – 36,000 feet) accounted for 20.9% of the global annual flight distance flown in 2019. However, given the limited sample size within this region (0 – 40°N and 28,000 – 36,000 feet, which collectively constitute only 14% of the full IAGOS dataset), we have opted against any attempts to rectify these biases.

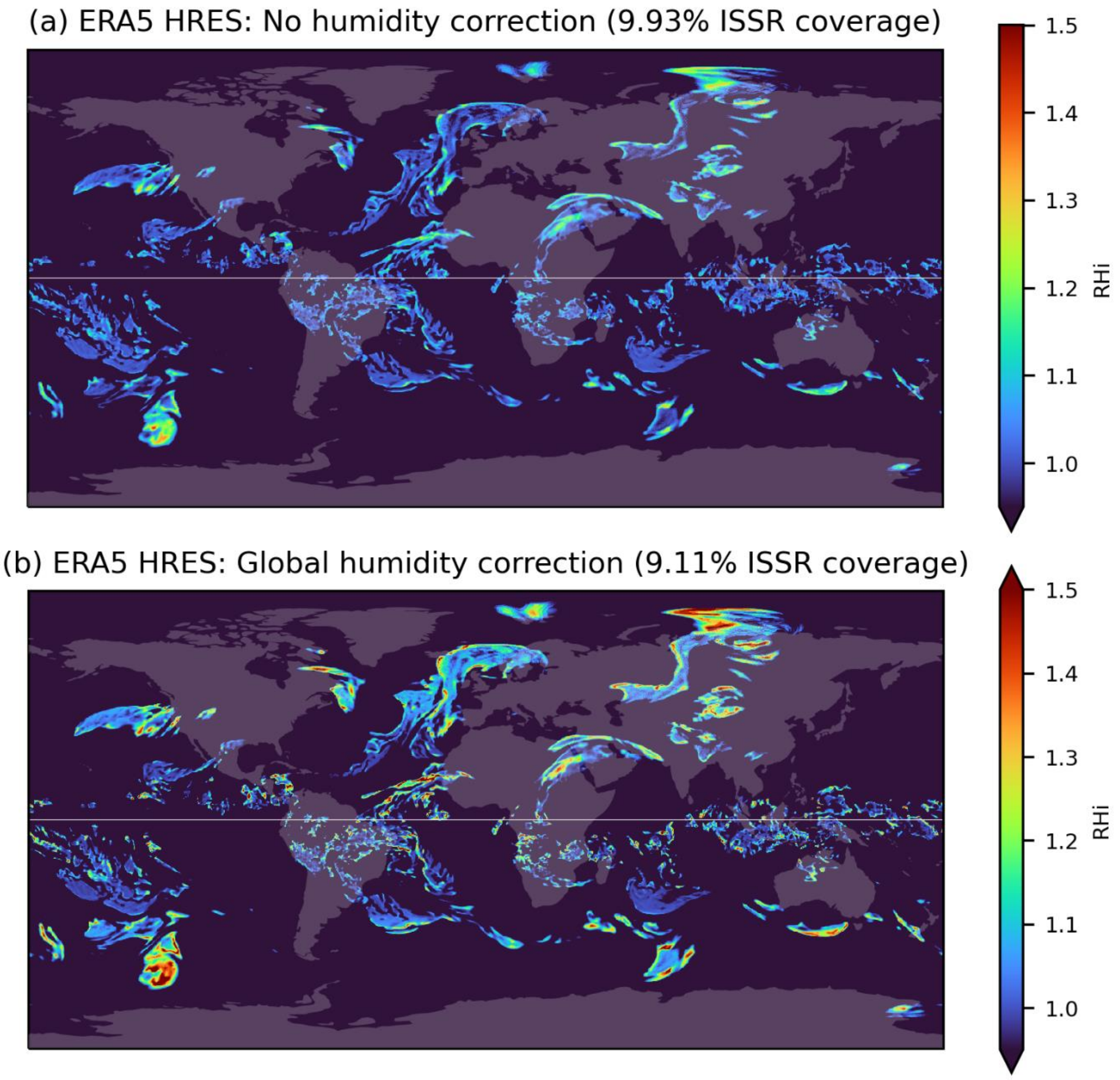

Figure S5: Comparison of the magnitude and spatial distribution of the: (a) original RHi fields provided by the ERA5 HRES; versus (b) the corrected RHi fields from the global humidity correction at pressure level 22500 Pa (36,000 feet) on 1-January-2020 00:00:00 (UTC). Basemap plotted using Cartopy 0.22.0 and sourced from Natural Earth; licensed under public domain.

Fig. S5 visualises the change in magnitude and spatial distribution of the uncorrected and corrected ERA5-derived humidity fields. It shows that the global humidity correction leads to: (i) a small reduction in ISSR coverage area at the tropics around the equator; (ii) an increase in ISSR coverage area at latitudes above 40°N and below 40°S; and (iii) a higher occurrence of localised regions with very high ice supersaturation (RHi > 140%). While the global humidity correction ensures that the RHi distribution derived from the ERA5 HRES is more consistent with RHi_{IAGOS} (Fig. S4), we note that: (i) there is a residual peak in $RHi_{corrected}$ at close to 1.0 (Fig. S4) because humidity in a waypoint is only scaled upwards when $a_{opt} < 1$ and $RHi_{waypoint} > (\frac{RHi}{a_{opt}})$; and (ii) RHi uncertainties at the individual waypoint level remains large (Fig. S6). Both issues should be addressed in future research.

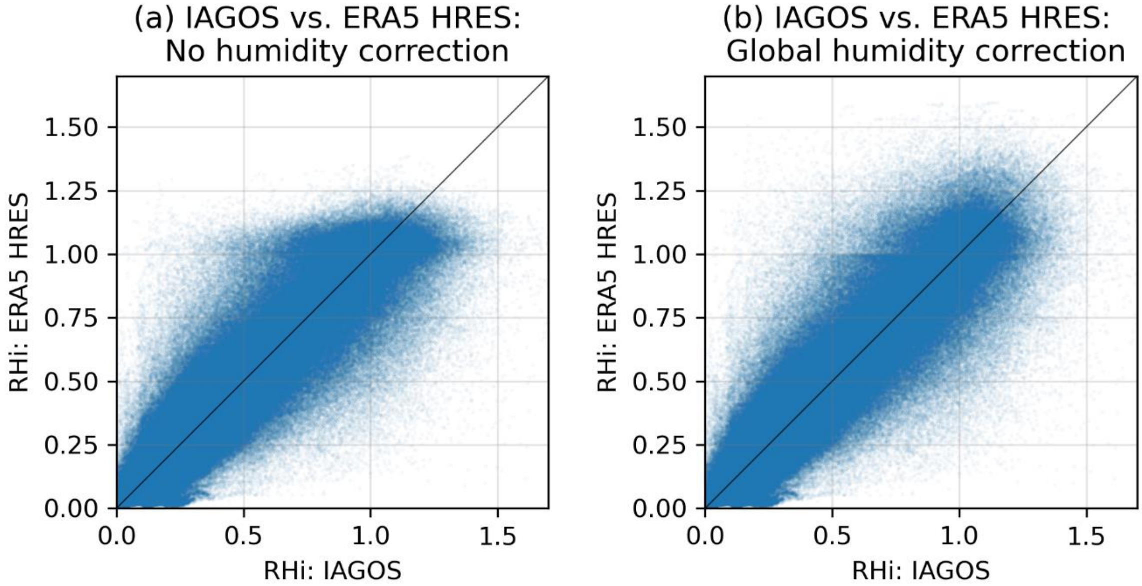

Figure S6: Parity plots comparing the RHi derived from in-situ measurements from the IAGOS campaign relative to: (a) the original RHi derived from the ERA5 HRES; and (b) the RHi when the global humidity correction is applied to the ERA5 HRES (n = 682,308).

S2 CoCiP model outputs

CoCiP is used to simulate the evolution and lifecycle of each contrail segment (Schumann, 2012; Schumann et al., 2012), and five different output formats are available:

- **contrail waypoint outputs**, which includes the local meteorology and simulated contrail properties at each contrail waypoint and provided at time steps of dt (300 s) from their formation to end of life,
- **flight waypoint outputs**, where the contrail waypoint outputs are aggregated back to the original flight waypoints,

- **flight level outputs**, where the flight waypoint outputs are aggregated for each flight,
- **time slice outputs**, where the contrail and flight waypoint outputs are summarised at time steps of 1 h, and
- **gridded outputs**, where the contrail and flight waypoint outputs are aggregated to a grid with a 0.5° × 0.5° horizontal resolution and at a 1 h temporal resolution.

In this study, we use the: (i) flight level and time slice outputs to derive the annual and seasonal statistics; (ii) gridded outputs to estimate the regional air traffic and contrail properties, where the spatial bounding boxes that defines each region were used in previous studies (Wilkerson et al., 2010; Hoare, 2014; Teoh et al., 2024) and reproduced in Table S5 and Fig. 2 in the main text; and (iii) contrail waypoint outputs to identify the set of conditions that produces strongly warming/cooling contrail segments.

Table S5: Spatial bounding boxes used to estimate the regional air traffic, emissions, and contrail properties.

Region	Bounding box				Surface area ($\times 10^{13}$ m^2)	Global surface area*
USA	(126° W,	23° N,	66° W,	50° N)	1.6005	3.1%
Europe	(12° W,	35° N,	20° E,	60° N)	0.6662	1.3%
East Asia	(103° E,	15° N,	150° E,	48° N)	1.6170	3.2%
Southeast Asia	(87.5° E,	10° S,	130° E,	20° N)	1.5533	3.1%
Latin America	(85° W,	60° S,	35° W,	15° N)	3.9774	7.8%
Africa & Middle East	(20° W,	35° S,	50° E,	40° N)	6.0334	12%
China	(73.5° E,	18° N,	135° E,	53.5° N)	2.1628	4.2%
India	(68° E,	8° N,	97.5° E,	35.5° N)	0.9244	1.8%
North Atlantic	(70° W,	40° N,	5° W,	63° N)	1.1493	2.3%
North Pacific	(140° E,	35° N,	120° W,	65° N)	2.3577	4.6%
Arctic Region	(180° W,	66.5° N,	180° E,	90° N)	2.1548	4.2%

* There are some overlapping between regional bounding boxes (Fig. 2 in the main text), and therefore, the summation of regional statistics does not add up to 100%.

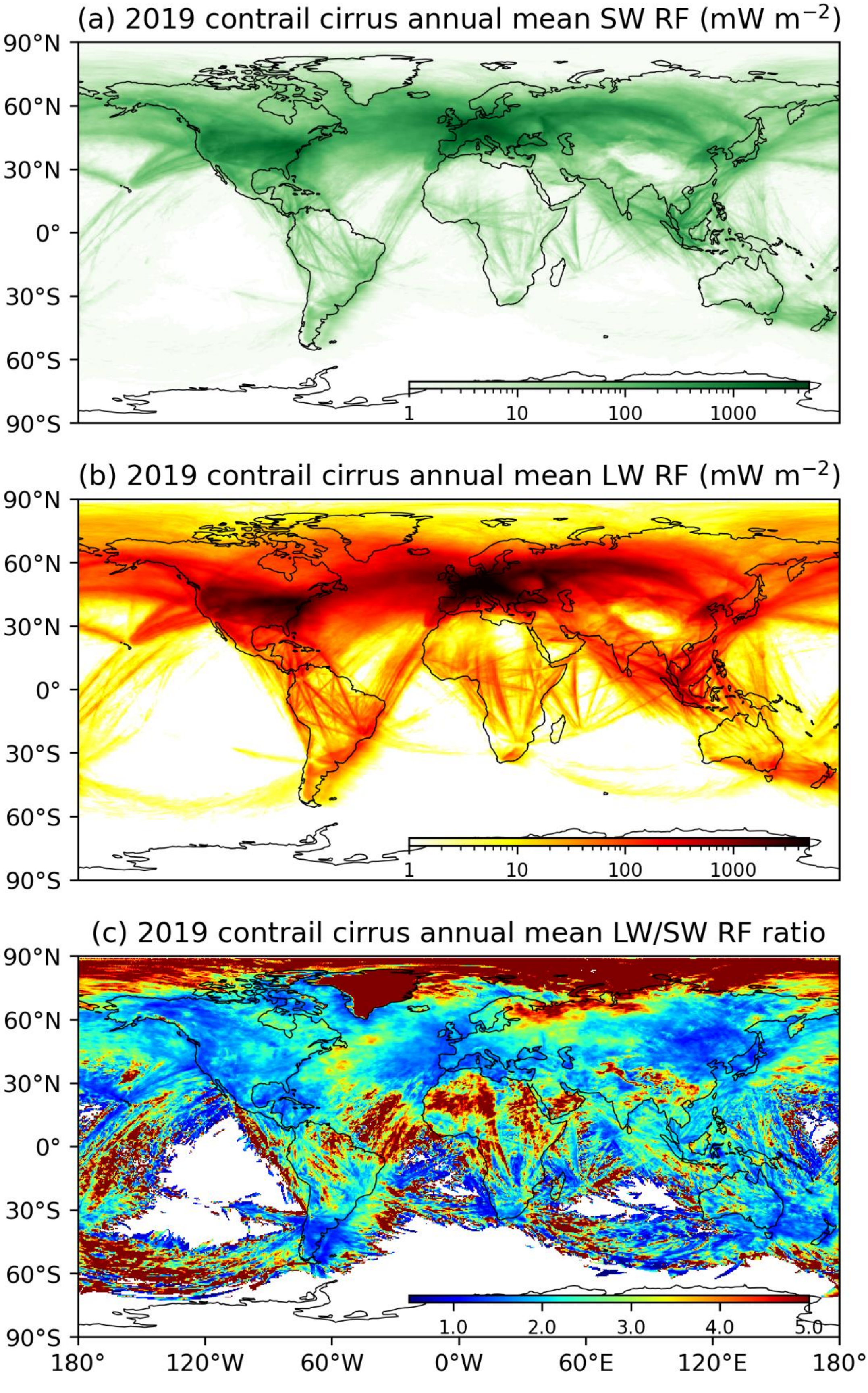

Figure S7: The 2019 global annual mean contrail cirrus: (a) SW RF; (b) LW RF; and (c) the ratio of LW-to-SW RF. Basemap plotted using Cartopy 0.22.0 and sourced from Natural Earth; licensed under public domain.

S3 Global contrail simulation

The global annual mean contrail cirrus net RF is estimated to be 62.1 mW m^{-2} in 2019, 27.3 mW m^{-2} in 2020, and 31.7 mW m^{-2} in 2021 with significant regional variabilities. Table 2 in the main text summarises the regional air traffic, emissions, and contrail statistics for 2019, while Tables S6 and S7 presents the same regional statistics for 2020 and 2021. Fig. 3a in the main text shows the global annual mean contrail cirrus net RF, while Fig. S7 shows the global annual mean contrail SW and LW RF and estimates the ratio of contrail LW-to-SW RF. One of the factors contributing to variability in the regional annual mean contrail net RF is the differences in air traffic patterns. Fig. S8 shows that: (i) flights over the North Atlantic are predominantly flown at cruising altitudes, which likely led to a larger percentage of flight distance forming persistent contrails ($p_{contrail}$); while (ii) flights in the Chinese airspace are generally flown at lower cruising altitudes, which could contribute to a smaller $p_{contrail}$.

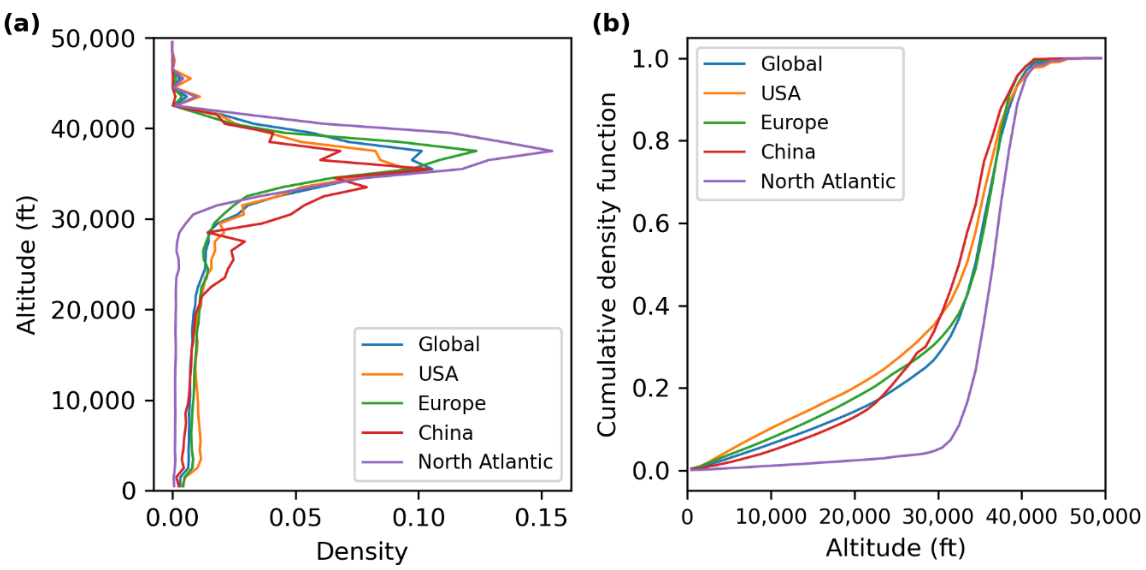

Figure S8: The (a) probability density function and (b) cumulative density function of the 2019 annual flight distance flown across the globe (blue lines) and over the USA (orange lines), Europe (green lines), China (red lines) and the North Atlantic (purple lines).

Table S6: Regional air traffic activity, emissions, and contrail properties for 2020.

Regional statistics: 2020	Global	USA	Europe	East Asia	SEA	Latin America	Africa & Middle East	China	India	North Atlantic	North Pacific	Arctic Region
Annual distance flown ($x10^9$ km)	34.50	11.27	3.592	6.298	1.569	1.071	2.015	6.848	1.257	1.159	1.615	0.1600
- Percentage relative to global values[a]	-	32.7%	10.4%	18.3%	4.5%	3.1%	5.8%	19.8%	3.6%	3.4%	4.7%	0.5%
Annual dist. flown above FL250 ($x10^9$ km)	26.33	7.84	2.742	4.372	1.227	0.852	1.714	4.846	1.040	1.111	1.352	0.1513
- Percentage relative to global values[a]	-	29.8%	10.4%	16.6%	4.7%	3.2%	6.5%	18.4%	3.9%	4.2%	5.1%	0.6%
Air traffic density (km^{-1} h^{-1})	0.008	0.080	0.062	0.044	0.012	0.003	0.004	0.036	0.016	0.012	0.008	0.001
Fuel burn (Tg)	146.000	32.400	14.600	29.500	7.730	4.450	9.910	31.600	6.200	6.830	10.800	1.140
Mean nvPM EI_n ($x10^{15}$ kg^{-1})	1.016	1.328	1.085	1.136	0.913	0.954	0.810	1.149	1.010	0.569	0.646	0.413
Mean nvPM per dist. ($x10^{12}$ m^{-1})	4.265	3.82	4.41	5.32	4.50	3.96	3.98	5.30	4.98	3.36	4.32	2.95
Persistent contrail length ($x10^9$ km)	1.40	0.429	0.237	0.0700	0.0618	0.0357	0.0493	0.0907	0.0215	0.107	0.0805	0.0193
- Percentage relative to global values[a]	-	30.6%	16.9%	5.0%	4.4%	2.5%	3.5%	6.5%	1.5%	7.6%	5.7%	1.4%
Dist. forming persistent contrails	4.07%	3.81%	6.60%	1.11%	3.94%	3.33%	2.45%	1.32%	1.71%	9.2%	4.98%	12.06%
Area-mean contrail optical depth, τ	0.014	0.043	0.049	0.020	0.014	0.012	0.011	0.020	0.015	0.027	0.020	0.023
Mean contrail age in domain (h)	2.34	1.97	2.01	2.46	2.98	3.04	2.66	2.48	2.58	2.36	2.64	3.98
Contrail cirrus coverage (%)	0.03	0.18	0.43	0.02	0.01	0.003	0.01	0.05	0.01	0.12	0.04	0.03
Contrail cirrus coverage, clear sky (%)	0.28	2.7	3.6	0.43	0.24	0.03	0.04	0.41	0.11	1.1	0.28	0.09
Annual mean SW RF (mW m^{-2})	-26.4	-241	-359	-40.1	-38.9	-6.54	-7.74	-42.7	-19.1	-77.2	-29.0	-3.69
Annual mean LW RF (mW m^{-2})	53.8	444	699	69.5	72.8	15.0	14.9	73.9	41.8	181	56.8	20.6
Annual mean Net RF (mW m^{-2})	27.3	203	339	29.3	33.8	8.42	7.15	31.2	22.6	104	27.7	17.0
Ratio: LW/SW RF	2.04	1.84	1.95	1.73	1.87	2.29	1.93	1.73	2.19	2.34	1.96	5.58
$EF_{contrail}$ ($x10^{18}$ J)	441	103	71.4	15.0	16.6	10.6	13.6	21.3	6.61	37.6	20.8	11.6
- Percentage relative to global values[a]	-	23.4%	16.2%	3.4%	3.8%	2.4%	3.1%	4.8%	1.5%	8.5%	4.7%	2.6%
$EF_{contrail}$, initial location ($x10^{18}$ J)[b]	441	106	79.4	15.0	16.8	10.7	13.7	20.2	6.41	39.3	21.1	9.18
- Percentage relative to global values[a]	-	24.0%	18.0%	3.4%	3.8%	2.4%	3.1%	4.6%	1.5%	8.9%	4.8%	2.1%
Ratio: $EF_{contrail}/EF_{contrail, initial}$[c]	1.00	0.97	0.90	1.00	0.99	0.99	0.99	1.05	1.03	0.96	0.99	1.26
$EF_{contrail}$ per flight distance ($x10^8$ J m^{-1})	0.128	0.094	0.221	0.024	0.107	0.100	0.068	0.029	0.051	0.339	0.131	0.574
$EF_{contrail}$ per contrail length ($x10^8$ J m^{-1})	3.14	2.47	3.35	2.14	2.72	3.00	2.78	2.23	2.98	3.67	2.62	4.76

[a]: There are some overlapping between regional bounding boxes (Fig. 2 in the main text), and therefore, the summation of regional statistics does not add up to 100%.

[b]: The total $EF_{contrail}$ throughout the contrail lifetime is added back to the location where contrails were initially formed.

[c]: A higher ratio indicates that a larger share of contrail climate forcing is from contrails initially formed outside of the region but subsequently advected into the domain.

Table S7: Regional air traffic activity, emissions, and contrail properties for 2021.

Regional statistics: 2021	Global	USA	Europe	East Asia	SEA	Latin America	Africa & Middle East	China	India	North Atlantic	North Pacific	Arctic Region
Annual distance flown (x10^9 km)	41.90	15.17	4.475	5.948	1.208	1.479	2.795	6.654	1.438	1.441	1.741	0.1930
- Percentage relative to global values[a]	-	36.2%	10.7%	14.2%	2.9%	3.5%	6.7%	15.9%	3.4%	3.4%	4.2%	0.5%
Annual dist. flown above FL250 (x10^9 km)	31.70	10.40	3.432	4.089	0.995	1.143	2.343	4.694	1.158	1.382	1.445	0.1791
- Percentage relative to global values[a]	-	32.8%	10.8%	12.9%	3.1%	3.6%	7.4%	14.8%	3.7%	4.4%	4.6%	0.6%
Air traffic density (km^{-1} h^{-1})	0.009	0.108	0.077	0.042	0.009	0.004	0.005	0.035	0.018	0.014	0.008	0.001
Fuel burn (Tg)	166.000	42.500	16.800	27.800	6.140	5.640	12.590	30.200	6.390	8.350	11.500	1.330
Mean nvPM EI_n (x10^{15} kg^{-1})	1.021	1.317	1.061	1.088	0.774	0.950	0.817	1.116	1.024	0.540	0.604	0.381
Mean nvPM per dist. (x10^{12} m^{-1})	4.009	3.69	3.98	5.09	3.93	3.62	3.68	5.06	4.55	3.13	3.99	2.62
Persistent contrail length (x10^9 km)	1.73	0.538	0.266	0.0813	0.0753	0.0568	0.0721	0.104	0.0328	0.137	0.1000	0.0140
- Percentage relative to global values[a]	-	31.1%	15.4%	4.7%	4.3%	3.3%	4.2%	6.0%	1.9%	7.9%	5.8%	0.8%
Dist. forming persistent contrails	4.13%	3.55%	5.94%	1.37%	6.23%	3.84%	2.58%	1.56%	2.28%	9.5%	5.74%	7.26%
Area-mean contrail optical depth, τ	0.012	0.046	0.046	0.021	0.014	0.012	0.010	0.020	0.015	0.027	0.021	0.022
Mean contrail age in domain (h)	2.25	1.91	1.93	2.47	3.06	3.16	2.55	2.48	2.56	2.35	2.62	3.72
Contrail cirrus coverage (%)	0.04	0.21	0.55	0.02	0.01	0.006	0.01	0.05	0.01	0.20	0.05	0.02
Contrail cirrus coverage, clear sky (%)	0.33	3.3	3.9	0.52	0.26	0.06	0.06	0.50	0.19	1.2	0.37	0.04
Annual mean SW RF (mW m^{-2})	-33.0	-304	-420	-47.8	-45.1	-10.0	-9.95	-50.5	-27.3	-104	-36.6	-4.18
Annual mean LW RF (mW m^{-2})	64.8	545	773	79.2	86.3	22.8	19.8	85.2	60.6	234	70.7	13.7
Annual mean Net RF (mW m^{-2})	31.7	240	352	31.3	41.1	12.8	9.79	34.7	33.2	130	34.0	9.56
Ratio: LW/SW RF	1.96	1.79	1.84	1.66	1.91	2.28	1.99	1.69	2.22	2.25	1.93	3.28
$EF_{contrail}$ (x10^{18} J)	511	121	74	15.9	20.1	16	18.6	23.6	9.67	47.1	25.4	6.51
- Percentage relative to global values[a]	-	23.7%	14.5%	3.1%	3.9%	3.1%	3.6%	4.6%	1.9%	9.2%	5.0%	1.3%
$EF_{contrail}$, initial location (x10^{18} J)[b]	511	125	77.2	16.1	20.3	16.5	19.5	21.8	9.63	48.7	25.3	5.26
- Percentage relative to global values[a]	-	24.5%	15.1%	3.2%	4.0%	3.2%	3.8%	4.3%	1.9%	9.5%	5.0%	1.0%
Ratio: $EF_{contrail}/EF_{contrail, initial}$[c]	1.00	0.97	0.96	0.99	0.99	0.97	0.95	1.08	1.00	0.97	1.00	1.24
$EF_{contrail}$ per flight distance (x10^8 J m^{-1})	0.122	0.082	0.173	0.027	0.168	0.112	0.070	0.033	0.067	0.338	0.145	0.273
$EF_{contrail}$ per contrail length (x10^8 J m^{-1})	2.95	2.32	2.90	1.98	2.70	2.90	2.70	2.10	2.94	3.55	2.53	3.76

[a]: There are some overlapping between regional bounding boxes (Fig. 2 in the main text), and therefore, the summation of regional statistics does not add up to 100%.

[b]: The total $EF_{contrail}$ throughout the contrail lifetime is added back to the location where contrails were initially formed.

[c]: A higher ratio indicates that a larger share of contrail climate forcing is from contrails initially formed outside of the region but subsequently advected into the domain.

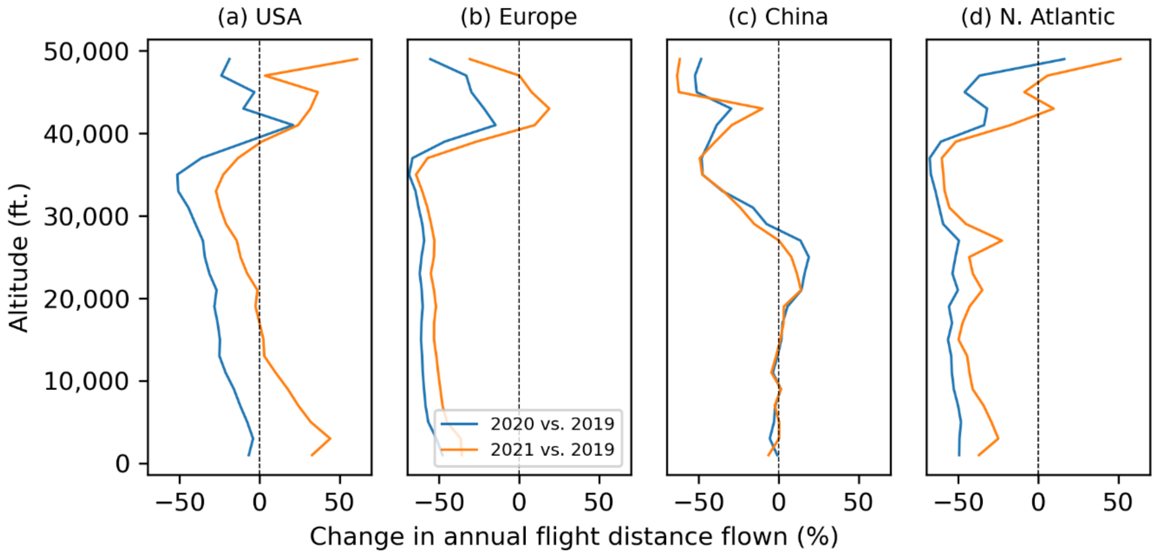

Figure S9: The percentage change in annual flight distance flown by altitude over the (a) USA; (b) Europe; (c) China; and (d) North Atlantic when comparing the air traffic in 2019 versus 2020 (blue lines) and 2021 (orange lines).

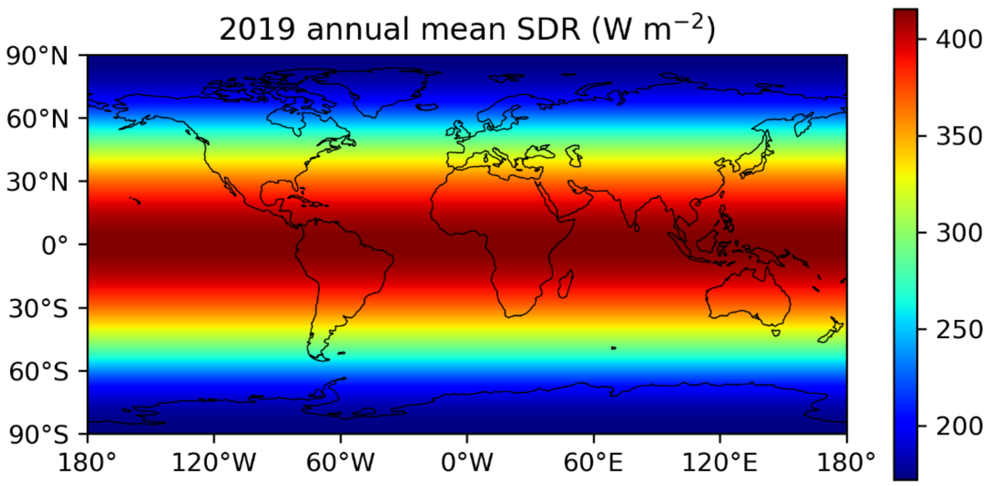

Figure S10: The 2019 global annual mean solar direct radiation that is provided by the ERA5 HRES. Basemap plotted using Cartopy 0.22.0 and sourced from Natural Earth; licensed under public domain.

Over the USA, Europe and North Atlantic, Fig. S9 shows that the COVID-19 pandemic led to significant reductions in air traffic activity between 20,000 and 40,000 feet, but there are only small changes in air traffic activity above 40,000 feet, likely due to a higher share of private business jets (ICAO, 2021; Sobieralski and Mumbower, 2022). The reduction in annual mean contrail net RF in East Asia and China (50 – 54%) is significantly larger than the change in flight distance flown (-24%), and this is most likely due to the: (i) lower share of international overflights which led to a 39% reduction in air traffic activity above 30,000 feet; and (ii) higher share of domestic air traffic in parts of China (Fig. 6a in the main text) that caused an 8% increase in flight distance flown between 25,000 and 30,000 feet (Fig. S9c) where persistent contrail formation is less likely.

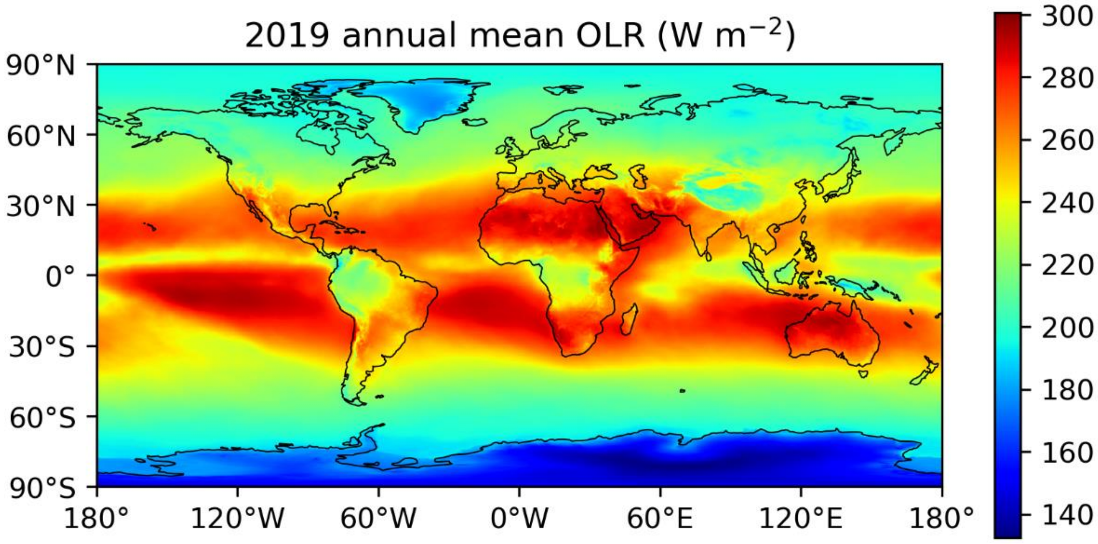

Figure S11: The 2019 global annual mean outgoing longwave radiation that is provided by the ERA5 HRES. Basemap plotted using Cartopy 0.22.0 and sourced from Natural Earth; licensed under public domain.

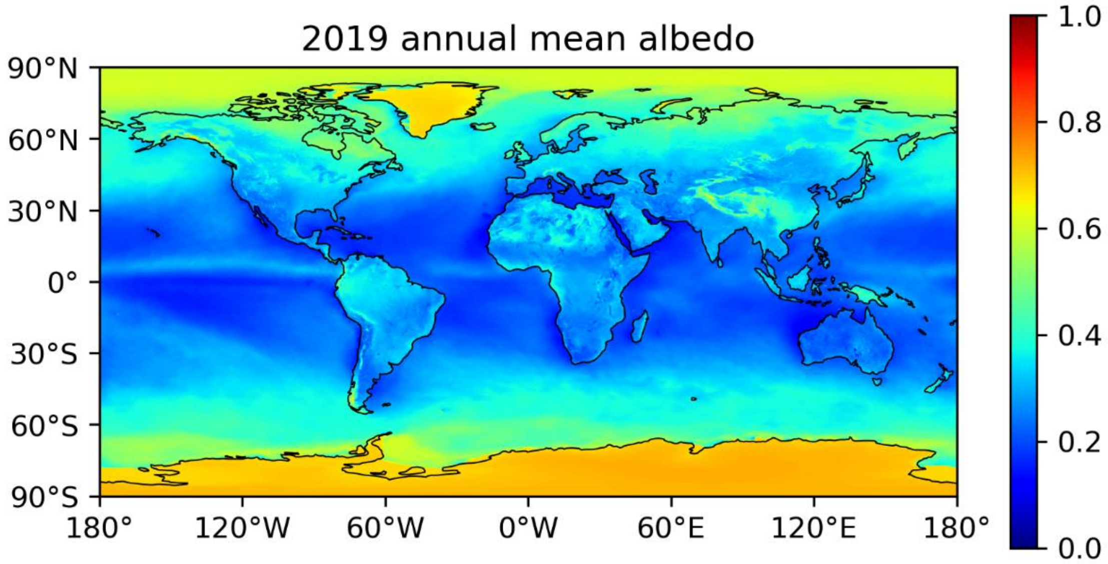

Figure S12: The 2019 global annual mean surface and cloud albedo as derived by dividing the annual mean reflected solar radiation by the solar direct radiation at each grid cell. Basemap plotted using Cartopy 0.22.0 and sourced from Natural Earth; licensed under public domain.

The solar direct radiation (SDR) and effective albedo, i.e., the proportion of solar radiation reflected by the surface and natural cirrus and calculated by dividing the reflected solar radiation (RSR) with the SDR, impact the contrail shortwave (SW) RF; while the magnitude of outgoing longwave radiation (OLR) influences the contrail longwave (LW) RF. Fig. S10 to S13 shows the spatial variations in global annual mean SDR, OLR, effective albedo, and the ratio of SDR-to-OLR, where: (i) the subtropics and Sahara Desert tends to have a high relative OLR (Fig. S11); (ii) the Arctic, Greenland and Antarctica have the highest effective albedo (Fig. S12); and (iii) Southeast Asia have the highest ratio of SDR-to-OLR (Fig. S13) which likely led to a higher probability of forming strongly cooling contrails. Fig. S14 shows the monthly-averaged ISSR occurrence at different latitude bins, represented as a percentage of the airspace volume. Notably, the ISSR occurrence at high latitudes (75°N - 90°N) exhibits a larger inter-annual variability relative to other latitude bands, likely due to its smaller grid cell area. Additionally, the ISSR occurrence between December 2019 and April 2020 is also around two times larger than the 2019–2021 annual averages. These factors, coupled with the low air traffic activity at high latitudes (0.62% and 0.06% of the global annual flight distance were flown above 66.5°N and below 45°S respectively), likely contributed to the large inter-annual variability in p_{contrail} between 2019 and 2021, as presented in Fig. 5 in the main text.

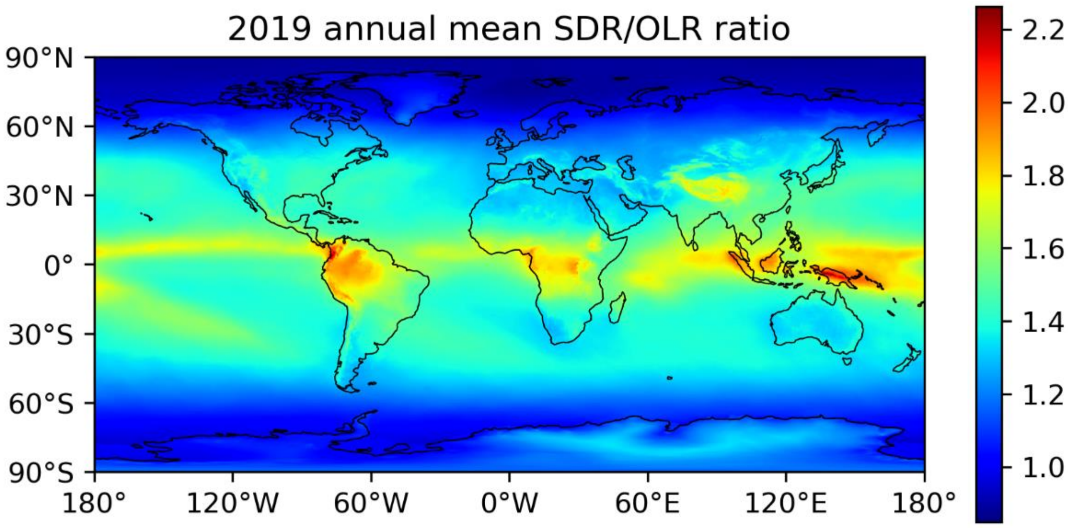

Figure S13: The ratio of the annual mean solar direct radiation (SDR) to the annual mean outgoing longwave radiation (OLR) for 2019, where the SDR and OLR are provided by the ERA5 HRES. Basemap plotted using Cartopy 0.22.0 and sourced from Natural Earth; licensed under public domain.

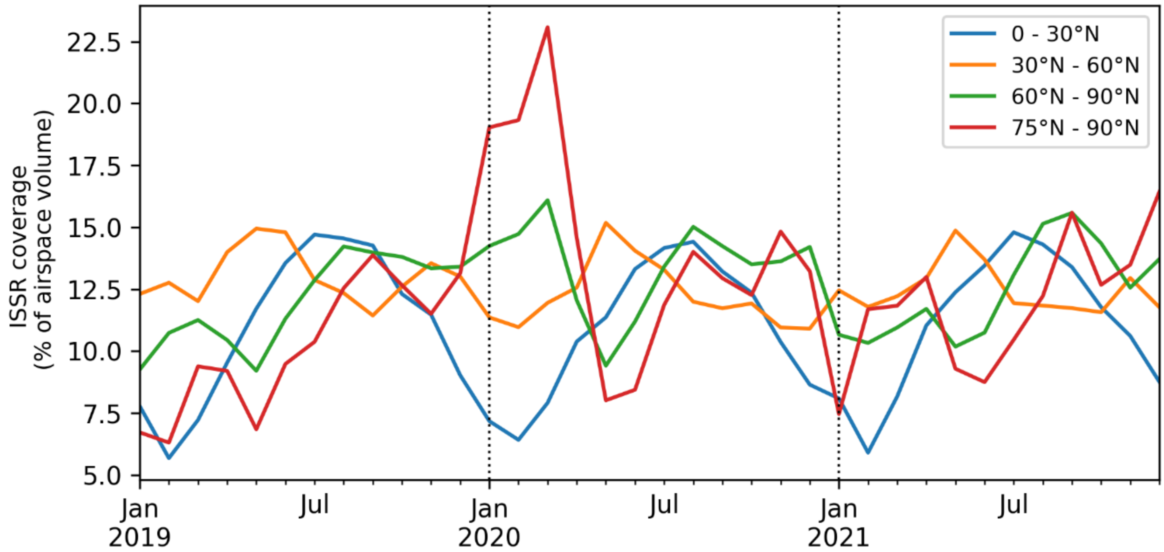

Figure S14: Monthly average ISSR coverage, expressed as a percentage of airspace volume, from 2019 to 2021 across at different latitude bands: 0 – 30°N (blue line), 30°N – 60°N (orange line), 60°N – 90°N (green line), and 75°N – 90°N (red line).

Fig. 7 in the main text and Fig. S15 summarises the seasonal variations in: (i) global annual flight distance flown; (ii) meteorological conditions where persistent contrails were initially formed; fleet-aggregated (iii) non-volatile particulate matter (nvPM) emissions; (iv) fraction of nvPM that formed ice crystals in persistent contrails; (v) mean contrail properties, such as the volume-mean ice crystal radius (r_{ice}), optical depth ($\tau_{contrail}$), lifetime, coverage area, and cloud-contrail overlap; and (vi) their associated RF and energy forcing ($EF_{contrail}$) per unit length of contrail.

Table S8: The threshold of $EF_{contrail}$ per flight distance flown by percentile.

Percentile	$EF_{contrail}$ per flight distance (J m^{-1})
1st	-7.11×10^8
5th	-2.39×10^8
33rd	1.00×10^6
50th	1.90×10^7
68th	1.97×10^8
95th	1.54×10^9
99th	2.85×10^9

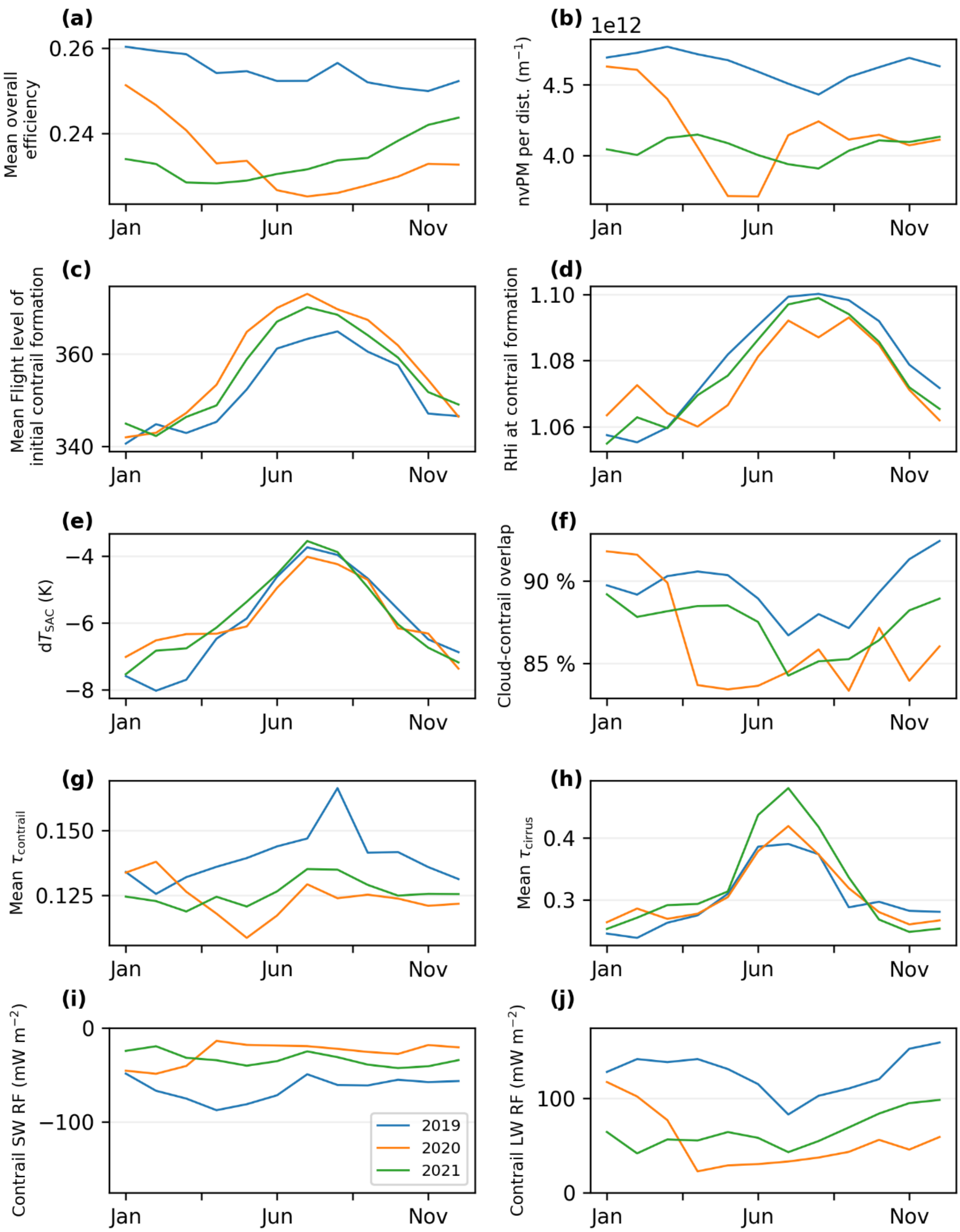

Figure S15: Monthly statistics on the: (a) global fleet-aggregated mean overall efficiency and (b) nvPM per flight distance flown; mean (c) flight level, (d) RHi, and (e) difference in the ambient temperature and Schmidt-Appleman criterion threshold temperature (dT_{SAC}) where contrails were initially formed; (f) mean percentage of cloud-contrail overlap; the lifetime mean (g) contrail optical depth ($\tau_{contrail}$) and (h) overlying natural cirrus optical depth (τ_{cirrus}); and the global annual mean contrail (i) SW RF and (j) LW RF.

Table S9: Top 20 origin-destination airport pairs that contribute to the strongly warming contrail segments ($EF_{contrail}$ per contrail length > 15.4 ×10^8 J m^{-1}, 95^{th} percentile) that were presented in Fig. 9 in the main text.

	Origin Airport	Destination Airport	% of flights*
1	John F Kennedy International Airport	London Heathrow Airport	0.65
2	Los Angeles International Airport	John F Kennedy International Airport	0.42
3	Washington Dulles International Airport	London Heathrow Airport	0.38
4	Ted Stevens Anchorage International Airport	Louisville Muhammad Ali International Airport	0.33
5	John F Kennedy International Airport	Los Angeles International Airport	0.32
6	San Francisco International Airport	John F Kennedy International Airport	0.30
7	Pointe-à-Pitre Le Raizet International Airport	Paris-Orly Airport	0.29
8	John F Kennedy International Airport	Adolfo Suárez Madrid–Barajas Airport	0.25
9	John F Kennedy International Airport	Charles de Gaulle International Airport	0.24
10	Orlando International Airport	London Gatwick Airport	0.23
11	Newark Liberty International Airport	London Heathrow Airport	0.23
12	Logan International Airport	Seattle Tacoma International Airport	0.22
13	Philadelphia International Airport	London Heathrow Airport	0.22
14	San Francisco International Airport	London Heathrow Airport	0.21
15	Adolfo Suárez Madrid–Barajas Airport	Licenciado Benito Juarez International Airport	0.21
16	Miami International Airport	London Heathrow Airport	0.21
17	Miami International Airport	Charles de Gaulle International Airport	0.20
18	Logan International Airport	Denver International Airport	0.20
19	Hartsfield Jackson Atlanta International Airport	Rome–Fiumicino Leonardo da Vinci International Airport	0.20
20	John F Kennedy International Airport	Malpensa International Airport	0.20

* Percentage of the subset of flights that formed strongly warming contrail segments

Table S10: Top 20 origin-destination airport pairs that contribute to the strongly cooling contrail segments ($EF_{contrail}$ per contrail length < -2.39 ×10^8 J m^{-1}, 5^{th} percentile) that were presented in Fig. 9 in the main text.

	Origin Airport	Destination Airport	% of flights*
1	Singapore Changi Airport	Suvarnabhumi Airport	0.61
2	Abu Dhabi International Airport	Soekarno-Hatta International Airport	0.54
3	Soekarno-Hatta International Airport	Narita International Airport	0.51
4	Singapore Changi Airport	Hong Kong International Airport	0.47
5	Dubai International Airport	Dallas Fort Worth International Airport	0.47
6	Sydney Kingsford Smith International Airport	Suvarnabhumi Airport	0.47
7	Brisbane International Airport	Singapore Changi Airport	0.46
8	Dubai International Airport	John F Kennedy International Airport	0.46
9	Dubai International Airport	Singapore Changi Airport	0.44
10	Dubai International Airport	Perth International Airport	0.43
11	Shanghai Pudong International Airport	Frankfurt am Main Airport	0.38
12	Dubai International Airport	Melbourne International Airport	0.37
13	Kuala Lumpur International Airport	Taiwan Taoyuan International Airport	0.36
14	Singapore Changi Airport	Brisbane International Airport	0.36
15	Kuala Lumpur International Airport	Soekarno-Hatta International Airport	0.36
16	Beijing Capital International Airport	Zürich Airport	0.36
17	Yuzhno-Sakhalinsk Airport	Novosibirsk Tolmachevo Airport	0.33
18	Sydney Kingsford Smith International Airport	Hong Kong International Airport	0.32
19	Soekarno-Hatta International Airport	Hong Kong International Airport	0.32
20	Incheon International Airport	Ninoy Aquino International Airport	0.32

* Percentage of the subset of flights that formed strongly cooling contrail segments

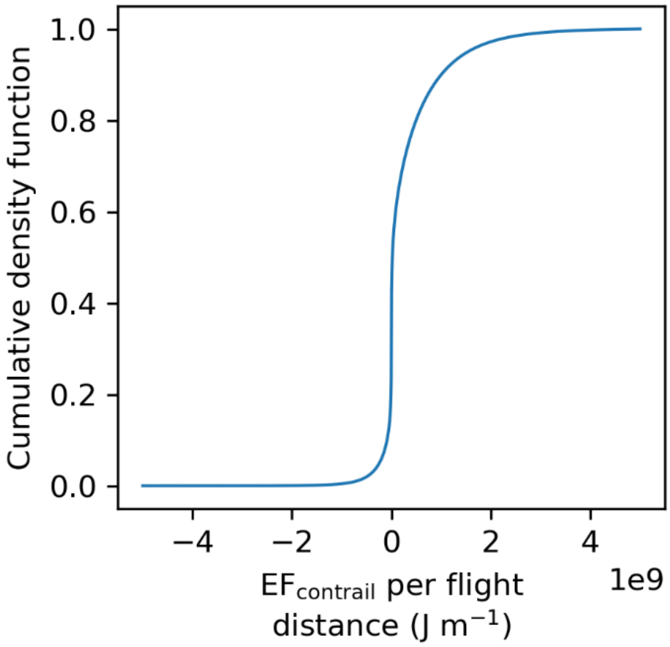

Figure S16: Cumulative density function of the magnitude of $EF_{contrail}$ per flight distance flown for every flight segment that formed persistent contrails in 2019. The percentiles of the $EF_{contrail}$ per flight distance is presented in Table S8.

Fig. S16 presents the cumulative density function of the $EF_{contrail}$ per flight distance flown for flight segments that formed persistent contrails in 2019. As every flight segment formed persistent contrails and the initial contrail length is equal to the flight segment length, the $EF_{contrail}$ per flight distance is expected to have the same magnitude as $EF_{contrail}$ per persistent contrail length. We use this data to define strongly warming contrail segments as those with $EF_{contrail}$ per contrail length greater than the 95th percentile ($> 15.4 \times 10^8$ J m^{-1}), while strongly cooling contrail segments have an $EF_{contrail}$ per contrail length below the 5th percentile ($< -2.39 \times 10^8$ J m^{-1}). Fig. 9a in the main text shows that the most strongly warming contrail segments are more prevalent over the US and North Atlantic, and Table S9 suggests that these contrail segments are generally formed by: (i) eastbound transatlantic flights from the North/South America to Europe and; (ii) transcontinental flights across the US, likely because these routes generally depart during the evenings (Teoh et al., 2022). In contrast, the most strongly cooling contrail segments are more common over Southeast Asia, Northern Asia, Europe, and the east of the North Atlantic (Fig. 9b in the main text) and Table S10 suggests that these contrails are formed by: (i) short-/medium-haul flights around Southeast and East Asia, likely because the region has a highest ratio of SDR to OLR relative to other regions; long-haul flights (ii) from the Middle East to Southeast Asia/Oceania and (iii) from Asia to Europe, likely due to flight scheduling factors where they have a higher probability of forming persistent contrails around dawn before they arrive to their destination; and (iv) westbound transatlantic air traffic activity that is generally highest during the morning (Teoh et al., 2022). Tables S9 and S10 also show that the top 20 origin-destination airport pairs accounted for: (i) 5.5% of the flights that formed strongly warming contrail segments; and (ii) 8.3% of the flights that formed strongly cooling contrail segments.

S4 Sensitivity analysis

Table S11 summarises the sensitivity of the simulated contrail properties and climate forcing to the corrections applied to the ERA5 HRES humidity fields, assumptions in aircraft-engine assignment and emissions, and contrail model parameters. Fig. S17 presents the global monthly mean contrail net RF from the different simulation runs, and shows that the percentage change in global monthly contrail net RF exhibits seasonal effects when comparing between the baseline simulation versus the simulation: (i) without humidity correction; (ii) with a constant humidity correction, c.f. Eq. (S5) where RHi_c = 0.95; (iii) with a constant nvPM EI_n of 10^{15} kg^{-1} for all waypoints; and (iv) without radiative heating interactions with the contrail plume.

Table S11: The 2019 global annual aviation fuel consumption, emissions, and contrail properties from the different model runs used in the sensitivity analysis.

2019 sensitivity analysis		Baseline	No humidity correction	Constant humidity correction (RHic = 0.95)	Default aircraft-engine: BADA	Constant nvPM EI_n (10^{15} kg^{-1})	Constant nvPM EI_n (10^{14} kg^{-1})	No radiative heating
Annual fuel burn	10^9 kg	280.1	280.1	280.1	279.2	280.1	280.1	280.1
Fuel burn per distance	kg km^{-1}	4.596	4.596	4.596	4.582	4.596	4.596	4.596
Annual CO_2 emissions	10^9 kg	884.8	884.8	884.8	882	884.8	884.8	884.8
Mean overall efficiency, η	-	0.297	0.302	0.297	0.297	0.297	0.297	0.297
Mean nvPM EI_n	10^{15} kg^{-1}	1.02	1.02	1.02	1.39	1	0.1	1.02
Mean nvPM per distance travelled	10^{12} m^{-1}	4.69	4.69	4.69	6.35	4.6	0.46	4.69
Flights forming contrails	%	42.53	42.13	42.56	42.58	42.53	42.53	42.53
Flights forming persistent contrails	%	23.78	21.88	24.92	23.79	23.78	23.82	23.88
Annual contrail length	10^9 km	21.35	21.25	21.45	21.37	21.35	21.35	21.35
Flight dist. forming contrails	%	35	34.9	35.2	35.1	35	35	35
Annual persistent contrail length	10^9 km	3.018	2.564	3.452	3.017	3.014	3.039	3.058
Flight dist. forming persistent contrails	%	4.95	4.21	5.66	4.95	4.95	4.99	5.02
Initial mean ice particle number per contrail length, $n_{ice,initial}$	10^{12} m^{-1}	2.5	2.22	2.45	3.31	2.25	0.22	2.5
Mean lifetime ice particle number per contrail length, n_{ice}	10^{12} m^{-1}	1.88	1.86	1.91	2.47	1.72	0.18	1.97
Mean contrail lifetime	h	2.43	2.21	2.44	2.56	2.56	1.66	3
Mean ice particle volume mean radius, r_{ice}	μm	9.96	7.82	9.12	9.19	9.03	14.1	8.5
Mean contrail segment optical depth, $\tau_{contrail}$	-	0.139	0.094	0.118	0.154	0.141	0.07	0.111
Mean contrail width	m	9903	8507	9864	10586	10521	5713	6875
Mean contrail depth	m	803	698	773	819	823	719	475
Contrail cirrus coverage	%	0.06	0.03	0.07	0.07	0.08	0.02	0.10
Contrail cirrus coverage, clear sky	%	0.66	0.37	0.66	0.74	0.86	0.08	0.60
Cloud-contrail overlap	%	90.2	91.8	89.8	90.6	90.7	67.5	83.1
Number of flights: warming contrails	-	6,741,548	6,034,669	7,041,971	6,693,704	6,721,659	7,031,761	6,922,105
Number of flights: cooling contrails	-	2,821,562	2,765,116	2,981,694	2,873,810	2,840,726	2,550,238	2,681,120
Ratio: warming-to-cooling contrails	-	2.39	2.18	2.36	2.33	2.37	2.76	2.58
Mean SW RF'	W m^{-2}	-4.15	-2.95	-3.72	-4.55	-4.19	-2.12	-3.49
Mean LW RF'	W m^{-2}	5.36	3.48	4.69	5.78	5.51	3.23	4.4
Mean net RF'	W m^{-2}	1.22	0.533	0.97	1.23	1.33	1.11	0.908
Annual mean SW RF	mW m^{-2}	-63.7	-36.1	-67.1	-74.5	-74.4	-13.5	-65.9
Annual mean LW RF	mW m^{-2}	126	70.9	132	148	149	27.3	133
Annual mean net RF	mW m^{-2}	62.1	34.8	64.5	73.1	74.8	13.7	66.8
Annual $EF_{contrail}$	10^{18} J	999	559	1038	1176	1204	221	1075
$EF_{contrail}$ per flight distance	10^8 J m^{-1}	0.164	0.092	0.17	0.193	0.198	0.036	0.176
$EF_{contrail}$ per contrail length	10^8 J m^{-1}	3.31	2.18	3.01	3.9	3.99	0.727	3.51
Flights responsible for 80% $EF_{contrail}$	%	2.68	2.23	2.89	2.81	2.66	2.65	2.92

Table S12: Comparison of the 2019 regional annual mean contrail SW, LW and net RF between the baseline simulation (with radiative heating and without contrail-contrail overlapping) versus the simulation that accounts for the radiative effects of contrail-contrail overlapping, and another simulation that without the effects of radiative heating interactions with the contrail plume.

Regional sensitivity analysis	Global	USA	Europe	East Asia	SEA	Latin America	Africa & Middle East	China	India	North Atlantic	North Pacific	Arctic Region
2019: Baseline simulation (Radiative heating effects ✓, contrail-contrail overlapping ✕)												
Annual mean SW RF (mW m^{-2})	-63.7	-485	-1160	-88.9	-83.8	-14.7	-20.0	-87.8	-35.6	-300	-55.0	-10.2
Annual mean LW RF (mW m^{-2})	126	900	2038	153	174	33.3	38.7	150	81.2	601	103	29.2
Annual mean Net RF (mW m^{-2})	62.1	414	876	63.9	90.4	18.5	18.6	62.3	45.4	300	47.7	19.0
2019 Sensitivity analysis: Contrail-contrail overlapping (Radiative heating effects ✓, contrail-contrail overlapping ✓)												
Annual mean SW RF (mW m^{-2})	-57.8	-435	-953	-84.4	-81.4	-14.7	-21.3	-85.2	-34.5	-281	-52.9	-9.94
Annual mean LW RF (mW m^{-2})	117	810	1750	146	169	33.2	41.5	148	78.9	571	99.8	28.4
Annual mean Net RF (mW m^{-2})	59.1	374	794	61.2	87.4	18.5	20.2	62.5	44.1	289	46.8	18.5
Change in SW RF	-9.3%	-10%	-18%	-5.1%	-2.9%	0.0%	6.5%	-3.0%	-3.1%	-6.3%	-3.8%	-2.5%
Change in LW RF	-7.1%	-10%	-14%	-4.6%	-2.9%	-0.3%	7.2%	-1.3%	-2.8%	-5.0%	-3.1%	-2.7%
Change in net RF	-4.8%	-9.7%	-9.4%	-4.2%	-3.3%	0.0%	8.6%	0.3%	-2.9%	-3.7%	-1.9%	-2.6%
2019 Sensitivity analysis: No radiative heating (Radiative heating effects ✕, contrail-contrail overlapping ✕)												
Annual mean SW RF (mW m^{-2})	-65.9	-452	-1214	-81.3	-82.0	-14.9	-22.1	-87.8	-36.1	-318	-56.7	-11.8
Annual mean LW RF (mW m^{-2})	133	874	2233	149	177	33.2	43.3	152	79.1	624	106	31.7
Annual mean Net RF (mW m^{-2})	66.8	420	1016	67.4	95.0	18.2	21.2	64.4	42.8	305	49.2	20.0
Change in SW RF	3.5%	-6.8%	4.7%	-8.5%	-2.1%	1.4%	11%	0.0%	1.4%	6.0%	3.1%	16%
Change in LW RF	5.6%	-2.9%	9.6%	-2.6%	1.7%	-0.3%	12%	1.3%	-2.6%	3.8%	2.9%	8.6%
Change in net RF	7.6%	1.4%	16%	5.5%	5.1%	-1.6%	14%	3.4%	-5.7%	1.7%	3.1%	5.3%

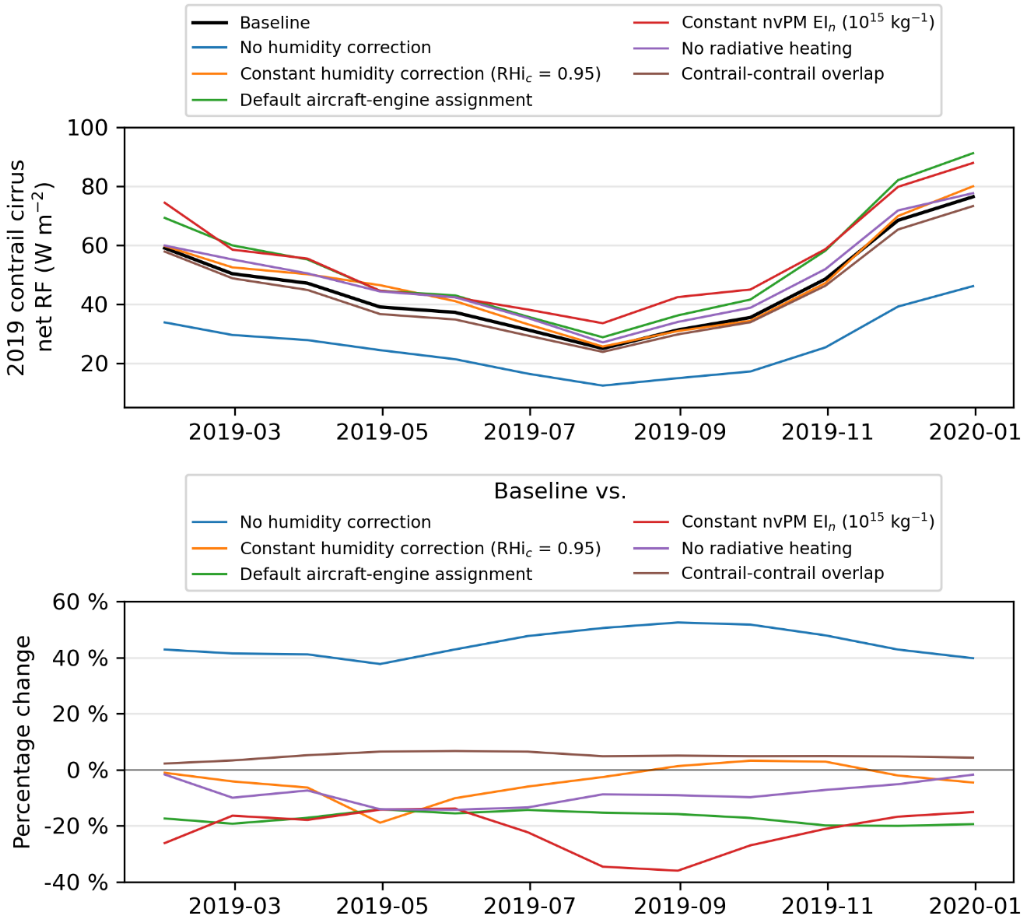

Figure S17: Comparison of the global monthly mean contrail net RF between the baseline scenario versus the simulation without humidity correction (blue lines), the simulation with default aircraft-engine assignments from BADA (orange lines), and the simulation without radiative heating effects (green lines).

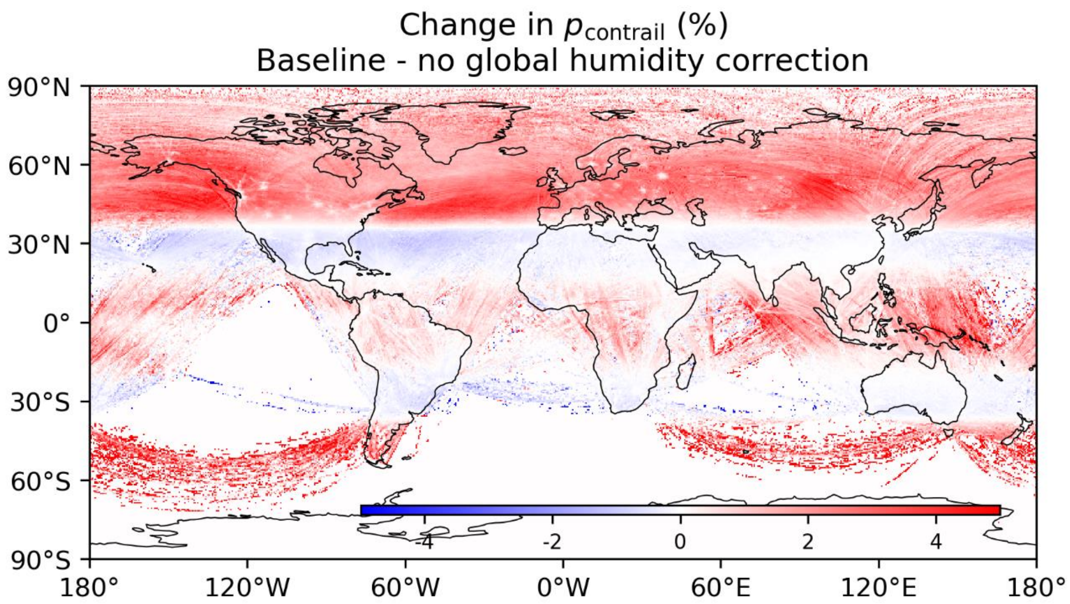

Figure S18: Change in the percentage of flight distance forming persistent contrails (p_{contrail}) for 2019 when comparing the baseline scenario with the simulation without global humidity corrections applied to the ERA5 HRES. Basemap plotted using Cartopy 0.22.0 and sourced from Natural Earth; licensed under public domain.

S4.1 Extended humidity correction

Fig. 10a in the main text shows significant latitude variations in the global annual mean contrail net RF when comparing between the baseline simulation with the extended global humidity corrections, c.f. Eq. (S6) to (S9) and described in Section S1.3, and the simulation without humidity corrections applied to the ERA5 HRES.

Over the tropics (25°S to 25°N), the extended humidity correction reduces the ISSR coverage ($a_{opt} > 1$, c.f. Eq. (S6) and Fig. S3a) but increases the RHi inside ISSRs ($b_{opt} \approx 3$, c.f. Eq. (S6) and Fig. S3b). When taken together, the extended humidity correction increases $p_{contrail}$ (from 2.4% without humidity correction to 2.6%, shown in Fig. S18) because a higher proportion of contrail segments survive the wake vortex phase, lifetime (+3.2%, from 2.50 to 2.58 h), and contrail net RF (+59%, from 32.9 to 52.3 mW m^{-2}). In the subtropics (30°N/S ± 5°), changes in $p_{contrail}$ (from 2.5% without humidity correction to 2.3%) and contrail net RF (+2.2%, from 82.4 to 84.2 mW m^{-2}) are small because effects from the smaller ISSR coverage ($a_{opt} > 1$) is balanced out by the smaller relative increase in RHi inside ISSRs ($b_{opt} \approx 1.5$). At latitudes above 35°N, the humidity correction increases the ISSR coverage ($a_{opt} < 1$) and RHi ($b_{opt} \approx 1.5$), both of which leads to significant increases in $p_{contrail}$ (from 5.7% to 7.1%) and contrail net RF (+96%, from 38.9 to 76.4 mW m^{-2}). A comparison of the $p_{contrail}$ by latitude for the simulation with and without humidity correction (Fig. S19) confirms that the minimum $p_{contrail}$ observed at the subtropics (30°N/S ± 5°) is not an artefact of the global humidity correction.

Seasonally, the difference in monthly contrail net RF is largest during the summer (+50% relative to the simulation without humidity correction) and smallest in wintertime (+40%) (Fig. S17), and this is likely caused by seasonal variations in the tropopause height thereby changing the proportion of flights cruising in the drier stratosphere that is not influenced by the humidity correction. We also evaluate the consistency in identifying the top 5% of flights with strongly warming contrails, where ~78% of flights with $EF_{contrail}$ > 95th percentile in the baseline simulation is also predicted to have an $EF_{contrail}$ > 95th percentile in the simulation without humidity correction.

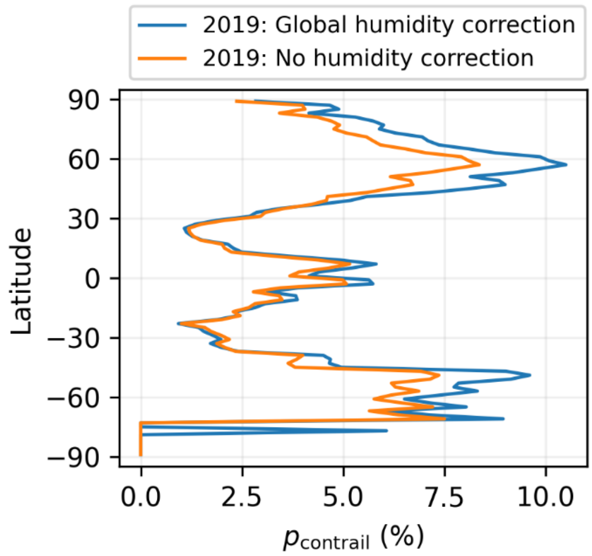

Figure S19: The percentage of annual flight distance flown that formed persistent contrails (pcontrail) in 2019 in the simulation with (blue line) and without (orange line) global humidity corrections applied to the ERA5 HRES (blue line).

S4.2 Radiative heating effects

Fig. 10e compare the difference in annual mean contrail cirrus net RF between the simulations with and without radiative heating effects and shows a: (i) larger contrail net RF along established flight corridors, because radiative heating increases the vertical mixing rate and $\tau_{contrail}$; and (ii) lower contrail net RF in regions that have a higher fraction of aged contrails, i.e., east coast of North and South America and away from established flight corridors (Fig. S20), because the solar and terrestrial radiation heats up the contrail plume and shortens its lifetime. Radiative heating also reduces the annual mean contrail net RF by 14% in Europe (Fig. 10e and Table S12) because less contrails are advected into the region via the North Atlantic jet stream.

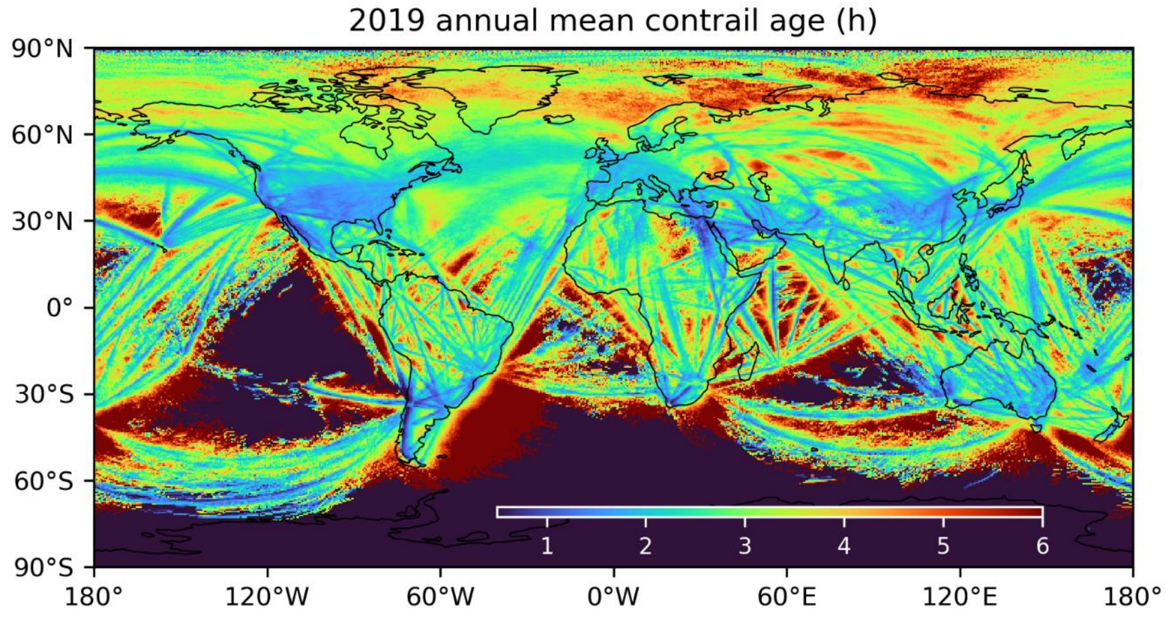

Figure S20: The 2019 global annual mean contrail age for the simulation without radiative heating interactions with the contrail plume. Basemap plotted using Cartopy 0.22.0 and sourced from Natural Earth; licensed under public domain.

S4.3 Contrail-contrail overlapping

Earlier studies suggested that the effects of contrail-contrail overlapping could lead to a 3% reduction in the annual mean contrail cirrus net RF globally (Sanz-Morère et al., 2021), and the contrail net RF could be reduced by up to 65% in regions with high air traffic density such as Europe (Schumann et al., 2021). CoCiP, when set up in its original form, does not account for the effects of contrail-contrail overlapping (Schumann, 2012; Schumann et al., 2012) but a recent regional study has attempted to approximate these effects with CoCiP by changing the background RSR and OLR fields resulting from the presence of contrails (Schumann et al., 2021).

In this study, we approximate the change in global and regional annual mean contrail net RF in 2019 due to contrail-contrail overlapping using an updated methodology of Schumann et al. (2021) and post-processing the contrail waypoint outputs from the 2019 baseline simulation. The contrail waypoint outputs provide information on each surviving contrail waypoint at a specific point in time, including the unique flight and waypoint identifier, the mid-point (longitude, latitude, and altitude), dimensions (length, width, and depth) and properties (ice crystal number, size, and optical depth) of contrail plume, and the local meteorology and radiation. Fundamentally, contrail-contrail overlapping changes the amount of solar and terrestrial radiation that reaches the contrail, where: (i) contrails at higher altitudes reflect part of the incoming SDR back to space, which reduces the amount of solar irradiance in reaching the contrails formed at lower altitudes; (ii) contrails at lower altitudes absorbs part of the OLR, causing contrails at higher altitudes to receive a smaller fraction of the OLR; and (iii) the SW component of the contrail RF at all altitudes increase the background RSR and cirrus albedo. On this basis, the radiative effects of contrail-contrail overlapping can be approximated by changing the background RSR and OLR fields, and the overlying cirrus optical depth above the contrail (τ_{cirrus}) so that these quantities, which are used as inputs to the parametric contrail RF model (Schumann et al., 2012), account for the presence of other contrails in a grid cell.

As CoCiP was run with model time steps (d*t*) of 300 s, there are 105,120 unique time slices in 2019. For each time slice, we: (i) obtain the global RSR and OLR fields at that specific time by interpolating the ERA5 HRES radiation fields; (ii) group contrail waypoints into altitude intervals of 500 m (~1640 feet); and (iii) process the contrail layers starting from the bottom to the top. All contrail segments found within each altitude interval, *k* (~500 m), are treated as one contrail layer where they do not overlap, and contrails above the layer under consideration (between *k* + 1 and the highest contrail layer *K*) are aggregated to update the τ_{cirrus},

$$(\tau_{\text{cirrus}})_{i,j} = \left(\tau_{\text{cirrus,ERA5 HRES}}\right)_{i,j} + \frac{\sum_{k+1}^{K}(\tau_{\text{contrail}} \times L \times W)_{i,j}}{A_{i,j}}, \qquad \text{(S10)}$$

where *i* and *j* represents the longitude and latitude of each grid cell, τ_{contrail} is the contrail segment optical depth, *L* and *W* are the contrail segment length and width, and *A* is the surface area of each grid cell. Collectively, each contrail layer also changes the background RSR and OLR fields,

$$\Delta \mathrm{RSR}_{i,j} = \frac{\Sigma\left(-\mathrm{RF}'_{\mathrm{SW,overlap}} \times L \times W\right)_{i,j}}{A_{i,j}}, \text{ and} \quad \text{(S11)}$$

$$\Delta \mathrm{OLR}_{i,j} = \frac{\Sigma\left(\mathrm{RF}'_{\mathrm{LW,overlap}} \times L \times W\right)_{i,j}}{A_{i,j}}, \quad \text{(S12)}$$

where the SW and LW RF' are computed with the updated RSR, OLR and τ_{cirrus} which accounts for the presence of other contrail cirrus, and the numerators are the sum of the contrail SW and LW radiative flux at each grid cell. Eq. (S10) to Eq. (S12) imply that: (i) the RSR and OLR received by contrails in the lowest layer (k = 1) is unchanged from the baseline simulation without contrail-contrail overlapping, but are expected to have a τ_{cirrus} that is larger than the baseline due to the presence of contrails above them; while (ii) contrails in the highest layer (k = K) are expected to have the same τ_{cirrus} as the baseline simulation, and a larger RSR (and albedo) and smaller OLR relative to the baseline simulation because of the presence of contrail cirrus below it. The updated RSR, OLR and τ_{cirrus} at each contrail waypoint are estimated using a bilinear interpolation across space (longitude and latitude). These are then used as inputs to the parametric contrail RF model (Schumann et al., 2012) to re-calculate the contrail SW and LW RF', which are subsequently used to estimate the $\mathrm{EF}_{\mathrm{contrail}}$ (Eq. (6) in the main text) and the global and regional annual mean contrail net RF (Eq. (7) in the main text) that accounts for contrail-contrail overlapping.

Using this approach, we estimate that the effects of contrail-contrail overlapping leads to a 5% reduction in the global annual mean contrail cirrus net RF (from 62.1 mW m^{-2} in the baseline simulation to 59.1 mW m^{-2}). Our estimated change in the 2019 global annual mean contrail net RF (-5%) is consistent with a parametric study that estimated a 3% reduction in the global contrail net RF due to contrail-contrail overlapping (Sanz-Morère et al., 2021). However, there are significant regional variations, where the reduction in annual mean contrail net RF is largest in regions with high air traffic activity, i.e., over the US (-9.7%) and Europe (-9.4%) (Fig. 10f in the main text and Table S12). The main factors contributing to the change in annual mean contrail net RF is evaluated in Fig. S21, suggesting that contrail-contrail overlapping tends to: (i) reduce the contrail climate forcing in grid cells with a large annual mean contrail net RF (> 1 W m^{-2}) and low ratio of annual mean contrail SW-to-LW RF (< 0.6); and (ii) increases the contrail climate forcing in grid cells with a low annual mean OLR (< 220 W m^{-2}) and high ratio of annual mean contrail SW-to-LW RF (> 0.6).

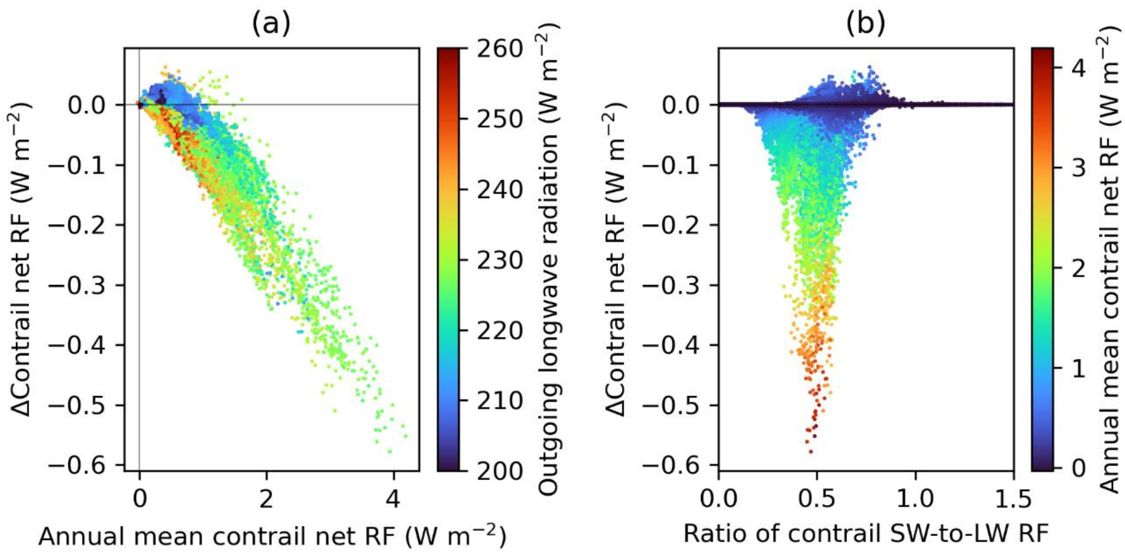

Figure S21: The change in contrail climate forcing at each grid cell (y-axis) due to contrail-contrail overlapping versus the: (a) annual mean contrail net RF (x-axis) and the annual mean outgoing longwave radiation (colour bar); and (b) ratio of annual mean contrail SW-to-LW RF (x-axis) and the annual mean contrail net RF (colour bar).

We note that this approach to approximate the radiative effects of contrail-contrail overlapping contains limitations and simplifying assumptions, where: (i) the change in background τ_{cirrus}, RSR, and OLR that is caused by each contrail, c.f. Eq. (S10) to (S12), is attributed to mid-point of the 3D contrail plume; (ii) it assumes maximum contrail-contrail overlapping across a vertical column in the 3D grid; and (iii) it does not account for the solar zenith angle, which can change the degree of overlapping, which in turn, changes the amount of solar radiation passing through each contrail layer. Thus, a more detailed evaluation of contrail-contrail overlapping that addresses these limitations is identified an avenue for future research.

S5 Comparison with other studies

Previous studies have used the 2002 AERO2K (Eyers et al., 2005) and 2006 Aviation Environmental Design Tool (AEDT) global aviation emissions inventories (Wilkerson et al., 2010) to simulate the global contrail climate forcing (Burkhardt and Kärcher, 2011; Chen and Gettelman, 2013; Schumann et al., 2015; Bock and Burkhardt, 2016; Bier and Burkhardt, 2022). A recent study from Lee et al. (2021) subsequently compiled the results from four studies (Burkhardt and Kärcher, 2011; Chen and Gettelman, 2013; Schumann et al., 2015; Bock and Burkhardt, 2016) and extrapolated the 2006 global contrail net RF to 2018 levels based on the growth in global annual flight distance flown. Table S13 summarises the methodological details and results from the different studies that quantified the global annual mean contrail cirrus net RF.

In the main text, we compared our 2019 global annual mean contrail net RF (62.1 mW m^{-2}) and ERF (26.1 mW m^{-2}) with the most recent studies from: (i) Lee et al. (2021), which estimated a 2018 global contrail net RF of 111 [33, 189] mW m^{-2} at a 95% confidence interval; (ii) Gettelman et al. (2021) which estimated a 2020 global contrail net ERF of 62 ± 59 mW m^{-2}, assuming an absence of the COVID-19 disruptions; and (iii) Bier & Burkhardt (2022), where the 2006 global contrail net RF from their previous study was revised down from 56 mW m^{-2} (Bock and Burkhardt, 2016) to 43.7 mW m^{-2} after accounting for differences in the nvPM activation rate and ice crystal losses in the wake vortex phase. The comparison with Bier & Burkhardt (2022) suggest that the average annual growth rate of the global contrail cirrus net RF, from 43.7 mW m^{-2} in 2006 (Bier and Burkhardt, 2022) to 62.1 mW m^{-2} (this study) amounting to +2.7% per annum between 2006 and 2019, was smaller than the growth in global annual flight distance flown during the same period (+3.6% per annum). The 3.6% average annual growth in flight distance flown was calculated based on the comparison of the 2006 values from the AEDT aviation emissions inventory (38.68 $\times10^9$ km) (Wilkerson et al., 2010) with the 2019 values (60.94 $\times10^9$ km) provided by the Global Aviation emissions Inventory based on ADS-B (GAIA) (Teoh et al., 2024).

Table S13: Summary of existing studies that quantified the global annual contrail cirrus net RF or ERF.

Study	Model	Air traffic data	Global annual mean contrail net RF or ERF (mW m^{-2})	Remarks
Burkhardt & Kärcher (2011)	ECHAM4	2002	37.5 (RF)	• Contrails initialised with dimensions of 100m (width) × 175 m (depth), and ice water content of 0.4 mg m^{-3}.
Chen & Gettelman (2013)	CAM5	2006	57 (RF)	• Contrails initialised with a 300 × 300m cross-sectional area, 7 µm ice particle diameter and spherical ice particle habits. • Results revised in Lee et al. (2021)
Schumann et al. (2015)	CoCiP-CAM3	2006	63 (RF)	• $RHi_{corrected}$ = RHi / 0.90 • Accounts for humidity exchange between contrails and the background air.
Bock & Burkhardt (2016)	ECHAM5	2006	56 (RF)	• Incorporated improved parameterisation of the contrail microphysical and optical properties from Lohmann et al. (2008), • Contrails initialised with constant ice crystal concentration of 150 cm^{-3}.
Lee et al. (2021)	Multi-model	2018	• 111 [33, 189] (RF) • 57.4 [17, 98] (ERF)	• Compiled the 2006 global annual mean contrail net RF from the above four studies and extrapolated to 2018 levels based on the growth in global air traffic. • RF range captures the uncertainty in: (i) contrail cirrus radiative response; and (ii) upper tropospheric water budget and the contrail cirrus scheme.
Gettelman et al. (2021)	CAM6	2020 (Assuming no COVID disruptions)	62 ± 59 (ERF)	• Scaled air traffic data from 2006 to 2020 levels assuming that: (i) the global air traffic distribution remains unchanged; and (ii) an absence of any COVID-19 disruptions. • Contrails initialised with a 100 m diameter, 7.5 µm ice particle diameter and spherical ice particle habits. • Accounts for the second-order contrail effects on background clouds
Bier & Burkhardt (2022)	ECHAM5	2006	44 [31, 49] (RF)	• Accounts for difference in nvPM activation rate and ice crystal losses in the wake vortex phase, • RF range captures the differences in initial soot assumptions of 1.5 [0.5, 3.0] $\times10^{15}$ kg^{-1}.

The AEDT aviation emissions inventory also reported the 2006 annual fuel consumption to be 188.2 $\times 10^9$ kg (Wilkerson et al., 2010), which we then use to derive the fuel consumption per flight distance flown (4.87 kg km^{-1}) and compare it with our estimates (4.60 kg km^{-1}). The nvPM EI_n was not reported in the AEDT, and we approximated the fleet-aggregated nvPM EI_n for 2006 (~1.15 $\times 10^{15}$ kg^{-1}) with GAIA by removing flights that are flown using new commercial aircraft types introduced after 2006 (i.e., Airbus A320neo, A350, A380 and the Boeing 737-MAX, 747-800 and 787 families). The absolute reduction in mean fuel consumption per flight distance flown (-6%) and nvPM EI_n (-11%) are expected to lower the number of nvPM emitted per flight distance flown, c.f. Eq. (5) in the main text, which subsequently reduces the $EF_{contrail}$ per flight distance flown (Teoh et al., 2022).

References

Agarwal, A., Meijer, V. R., Eastham, S. D., Speth, R. L., and Barrett, S. R. H.: Reanalysis-driven simulations may overestimate persistent contrail formation by 100-250%, Environmental Research Letters, 17, 1–14, https://doi.org/10.1088/1748-9326/AC38D9, 2022.

Bier, A. and Burkhardt, U.: Impact of Parametrizing Microphysical Processes in the Jet and Vortex Phase on Contrail Cirrus Properties and Radiative Forcing, Journal of Geophysical Research: Atmospheres, 127, e2022JD036677, https://doi.org/10.1029/2022JD036677, 2022.

Bock, L. and Burkhardt, U.: Reassessing properties and radiative forcing of contrail cirrus using a climate model, Journal of Geophysical Research: Atmospheres, 121, 9717–9736, https://doi.org/10.1002/2016JD025112, 2016.

Boulanger, D., Bundke, U., Gallagher, M., Gerbig, C., Hermann, M., Nédélec, P., Rohs, S., Sauvage, B., Ziereis, H., Thouret, V., and Petzold, A.: IAGOS Time series [Data set], AERIS, https://doi.org/https://doi.org/10.25326/06, 2022.

Burkhardt, U. and Kärcher, B.: Global radiative forcing from contrail cirrus, Nat Clim Chang, 1, 54–58, https://doi.org/10.1038/nclimate1068, 2011.

Chen, C. C. and Gettelman, A.: Simulated radiative forcing from contrails and contrail cirrus, Atmos Chem Phys, 13, 12525–12536, https://doi.org/10.5194/acp-13-12525-2013, 2013.

ECMWF: The Copernicus Programme: Climate Data Store, https://cds.climate.copernicus.eu/#!/home, 2021. Last access: 15 February 2022.

Eyers, C. J., Addleton, D., Atkinson, K., Broomhead, M. J., Christou, R., Elliff, T., Falk, R., Gee, I., Lee, D. S., Marizy, C., Michot, S., Middel, J., Newton, P., Norman, P., Plohr, M., Raper, D., and Stanciou, N.: AERO2K global aviation emissions inventories for 2002 and 2025, QinetiQ for European Commission under Contract No. G4RD-CT-2000-00382, Farnborough, Hampshire, GU14 0LX, pp., 2005., 2005.

Gettelman, A., Chen, C. C., and Bardeen, C. G.: The climate impact of COVID-19-induced contrail changes, Atmos Chem Phys, 21, 9405–9416, https://doi.org/10.5194/ACP-21-9405-2021, 2021.

Gierens, K., Matthes, S., and Rohs, S.: How Well Can Persistent Contrails Be Predicted?, Aerospace, 7, 169, https://doi.org/10.3390/AEROSPACE7120169, 2020.

Hersbach, H., Bell, B., Berrisford, P., Hirahara, S., Horányi, A., Muñoz-Sabater, J., Nicolas, J., Peubey, C., Radu, R., Schepers, D., Simmons, A., Soci, C., Abdalla, S., Abellan, X., Balsamo, G., Bechtold, P., Biavati, G., Bidlot, J., Bonavita, M., De Chiara, G., Dahlgren, P., Dee, D., Diamantakis, M., Dragani, R., Flemming, J., Forbes, R., Fuentes, M., Geer, A., Haimberger, L., Healy, S., Hogan, R. J., Hólm, E., Janisková, M., Keeley, S., Laloyaux, P., Lopez, P., Lupu, C., Radnoti, G., de Rosnay, P., Rozum, I., Vamborg, F., Villaume, S., and Thépaut, J. N.: The ERA5 global reanalysis, Quarterly Journal of the Royal Meteorological Society, 146, 1999–2049, https://doi.org/10.1002/qj.3803, 2020.

Hoare. G: Country bounding boxes, https://gist.github.com/graydon/11198540, 2014. Last access: 22 December 2022.

ICAO: The World of Air Transport in 2020, https://www.icao.int/annual-report-2020/Pages/the-world-of-air-transport-in-2020.aspx, 2021. Last access: 15 August 2022

Kärcher, B. and Lohmann, U.: A parameterization of cirrus cloud formation: Homogeneous freezing of supercooled aerosols, Journal of Geophysical Research: Atmospheres, 107, AAC 4-1, https://doi.org/10.1029/2001JD000470, 2002.

Koop, T., Luo, B., Tsias, A., and Peter, T.: Water activity as the determinant for homogeneous ice nucleation in aqueous solutions, Nature, 406, 611–614, https://doi.org/10.1038/35020537, 2000.

Lee, D. S., Fahey, D. W., Skowron, A., Allen, M. R., Burkhardt, U., Chen, Q., Doherty, S. J., Freeman, S., Forster, P. M., Fuglestvedt, J., Gettelman, A., De León, R. R., Lim, L. L., Lund, M. T., Millar, R. J., Owen, B., Penner, J. E., Pitari, G., Prather, M. J., Sausen, R., and Wilcox, L. J.: The contribution of global aviation to anthropogenic climate forcing for 2000 to 2018, Atmos Environ, 244, 117834, https://doi.org/10.1016/J.ATMOSENV.2020.117834, 2021.

Lohmann, U., Spichtinger, P., Jess, S., Peter, T., and Smit, H.: Cirrus cloud formation and ice supersaturated regions in a global climate model, Environmental Research Letters, 3, 045022, https://doi.org/10.1088/1748-9326/3/4/045022, 2008.

Parr, W. C. and Schucany, W. R.: Minimum distance and robust estimation, J Am Stat Assoc, 75, 616–624, https://doi.org/10.1080/01621459.1980.10477522, 1980.

Petzold, A., Neis, P., Rütimann, M., Rohs, S., Berkes, F., G. J. Smit, H., Krämer, M., Spelten, N., Spichtinger, P., Nédélec, P., and Wahner, A.: Ice-supersaturated air masses in the northern mid-latitudes from regular in situ observations by passenger aircraft: Vertical distribution, seasonality and tropospheric fingerprint, Atmos Chem Phys, 20, 8157–8179, https://doi.org/10.5194/ACP-20-8157-2020, 2020.

Pruppacher, H. R., Klett, J. D., and Wang, P. K.: Microphysics of Clouds and Precipitation, http://dx.doi.org/10.1080/02786829808965531, 28, 381–382, https://doi.org/10.1080/02786829808965531, 2007.

Reutter, P., Neis, P., Rohs, S., and Sauvage, B.: Ice supersaturated regions: Properties and validation of ERA-Interim reanalysis with IAGOS in situ water vapour measurements, Atmos Chem Phys, 20, 787–804, https://doi.org/10.5194/ACP-20-787-2020, 2020.

Santer, B. D., Sausen, R., Wigley, T. M. L., Boyle, J. S., AchutaRao, K., Doutriaux, C., Hansen, J. E., Meehl, G. A., Roeckner, E., Ruedy, R., Schmidt, G., and Taylor, K. E.: Behavior of tropopause height and atmospheric temperature in models, reanalyses, and observations: Decadal changes, Journal of Geophysical Research: Atmospheres, 108, ACL 1-1, https://doi.org/10.1029/2002JD002258, 2003.

Sanz-Morère, I., Eastham, S. D., Allroggen, F., Speth, R. L., and Barrett, S. R. H.: Impacts of multi-layer overlap on contrail radiative forcing, Atmos Chem Phys, 21, 1649–1681, https://doi.org/10.5194/ACP-21-1649-2021, 2021.

Schumann, U.: A contrail cirrus prediction model, Geosci Model Dev, 5, 543–580, https://doi.org/10.5194/gmd-5-543-2012, 2012.

Schumann, U., Mayer, B., Graf, K., and Mannstein, H.: A parametric radiative forcing model for contrail cirrus, J Appl Meteorol Climatol, 51, 1391–1406, https://doi.org/10.1175/JAMC-D-11-0242.1, 2012.

Schumann, U., Penner, J. E., Chen, Y., Zhou, C., and Graf, K.: Dehydration effects from contrails in a coupled contrail–climate model, Atmos Chem Phys, 15, 11179–11199, https://doi.org/10.5194/acp-15-11179-2015, 2015.

Schumann, U., Poll, I., Teoh, R., Koelle, R., Spinielli, E., Molloy, J., Koudis, G. S., Baumann, R., Bugliaro, L., Stettler, M., and Voigt, C.: Air traffic and contrail changes over Europe during COVID-19: A model study, Atmos Chem Phys, 21, 7429–7450, https://doi.org/10.5194/ACP-21-7429-2021, 2021.

Sobieralski, J. B. and Mumbower, S.: Jet-setting during COVID-19: Environmental implications of the pandemic induced private aviation boom, Transp Res Interdiscip Perspect, 13, 100575, https://doi.org/10.1016/J.TRIP.2022.100575, 2022.

Sonntag, D.: Advancements in the field of hygrometry, Meteorologische Zeitschrift, 3, 51–66, https://doi.org/10.1127/metz/3/1994/51, 1994.

Teoh, R., Schumann, U., Majumdar, A., and Stettler, M. E. J.: Mitigating the Climate Forcing of Aircraft Contrails by Small-Scale Diversions and Technology Adoption, Environ Sci Technol, 54, 2941–2950, https://doi.org/10.1021/acs.est.9b05608, 2020.

Teoh, R., Schumann, U., Gryspeerdt, E., Shapiro, M., Molloy, J., Koudis, G., Voigt, C., and Stettler, M.: Aviation Contrail Climate Effects in the North Atlantic from 2016-2021., Atmos. Chem. Phys., 22, 10919–10935, https://doi.org/https://doi.org/10.5194/acp-2022-169, 2022.

Teoh, R., Engberg, Z., Shapiro, M., Dray, L., and Stettler, M. E. J.: The high-resolution Global Aviation emissions Inventory based on ADS-B (GAIA) for 2019–2021, Atmos Chem Phys, 24, 725–744, https://doi.org/10.5194/ACP-24-725-2024, 2024.

Tompkins, A. M., Gierens, K., and Rädel, G.: Ice supersaturation in the ECMWF integrated forecast system, Quarterly Journal of the Royal Meteorological Society, 133, 53–63, https://doi.org/10.1002/qj.14, 2007.

Wilkerson, J. T., Jacobson, M. Z., Malwitz, A., Balasubramanian, S., Wayson, R., Fleming, G., Naiman, A. D., and Lele, S. K.: Analysis of emission data from global commercial aviation: 2004 and 2006, Atmos Chem Phys, 10, 6391–6408, https://doi.org/10.5194/acp-10-6391-2010, 2010.